

# Merkel Cell Carcinoma Sensitivity to EZH2 Inhibition Is Mediated by SIX1 Derepression

Ashley K. Gartin<sup>1,2</sup>, Thomas C. Frost<sup>1,2</sup>, Camille H. Cushman<sup>1,2</sup>, Brittaney A. Leeper<sup>3,4</sup>, Prafulla C. Gokhale<sup>3,4</sup> and James A. DeCaprio<sup>1,2,5</sup>

Polycomb repressive complex 2 has a critical role in the maintenance of bivalent promoters and is often perturbed in cancer, including neuroendocrine tumors. In this study, we investigated the susceptibility of Merkel cell carcinoma (MCC), a neuroendocrine carcinoma of the skin, to inhibitors of the Polycomb repressive complex 2 catalytic subunit EZH2. We show that a subset of MCC cell lines is sensitive to EZH2 inhibitor-induced cell viability loss. We find that inhibitor treatment of susceptible cells derepresses the Polycomb repressive complex 2 target *SIX1*, a transcription factor in the PAX-SIX-EYA-DACH network normally involved in inner ear hair cell development, and that PAX-SIX-EYA-DACH network transcription factors are critical contributors to EZH2 inhibitor-induced MCC cell viability loss. Furthermore, we show the EZH2 inhibitor tazemetostat slows the growth of MCC xenografts and derepresses *SIX1* and its downstream inner ear transcriptional target *MYO6* in vivo. We propose that EZH2 inhibition in MCC leads to *SIX1* derepression with dysregulation of hearing-related transcriptional programs and growth inhibition. This study provides evidence that MCC tumors may be specifically susceptible to EZH2 inhibitors, while giving mechanistic insight into the transcriptional programs these inhibitors perturb in MCC, and potentially in other neuroendocrine cancers.

*Journal of Investigative Dermatology* (2022) ■, ■–■; doi:10.1016/j.jid.2022.03.008

## INTRODUCTION

Polycomb repressive complex 2 (PRC2) contains one of the methyltransferases EZH1 or EZH2 and deposits histone H3 lysine 27 (H3K27) methylation. Promoter-associated H3K27 di- and trimethylation (H3K27me3) is repressive, whereas H3K27me3 and histone H3 lysine 4 trimethylation (H3K4me3) together denote potentially reactivatable bivalent promoters (Blanco et al., 2020). PRC2 dysregulation through *EZH2* gain-of-function mutations (Knutson et al., 2014; McCabe et al., 2012) or loss of opposing SWI/SNF activity (Knutson et al., 2013; Wilson et al., 2010) sensitizes tumors to EZH2 inhibitors (EZH2i). Among these, tazemetostat is approved therapy for follicular lymphoma and epithelioid sarcoma carrying the aforementioned mutations (Italiano et al., 2018). PRC2 subunit overexpression also correlates with aggressiveness of many tumors, including

neuroendocrine carcinomas like small cell lung cancer (Byers et al., 2012; Sato et al., 2013) and neuroendocrine prostate cancer (Dardenne et al., 2016), and creates a similar EZH2i vulnerability (Kruger et al., 2017).

Merkel cell carcinoma (MCC) is a neuroendocrine skin carcinoma with two etiologies. Nonviral MCC typically exhibits UV mutagenesis of *RB1* and *TP53* (Wong et al., 2015). Viral MCC is caused by Merkel cell polyomavirus DNA integration and T antigen expression, which inhibits RB1 and p53 activity (Hesbacher et al., 2016; Park et al., 2019). MCC also exhibits epigenetic dysregulation. In nonviral MCC, *KMT2D* is frequently mutated (Starrett et al., 2020). In viral MCC, small T antigen upregulates *KDM1A* resulting in LSD1 inhibitor sensitivity (Leiendecker et al., 2020; Park et al., 2020). Furthermore, HDAC inhibitors increase MCC antigen presentation machinery expression, raising surface levels of major histocompatibility complex class I (Ritter et al., 2017; Song et al., 2021) and enhancing T-cell infiltration (Ugurel et al., 2019). PRC2 may also be dysregulated in MCC, as tumors overexpress *EZH2* relative to normal skin (Veija et al., 2017) and EZH2 levels correlate with prognosis (Harms et al., 2017). In addition, EZH2i raised surface levels of major histocompatibility complex class I in one MCC cell line (Burr et al., 2019). However, a full understanding of PRC2's role in MCC is lacking.

Among the initially described bivalent genes were members of the PAX-SIX-EYA-DACH transcription factor (TF) network (PSEDN) (Bernstein et al., 2006). SIX proteins bind DNA (Li et al., 2020), whereas EYAs contain a transactivation domain (Liu et al., 2016). SIX–EYA complexes are generally transcriptional activators, although SIX can also be a repressor. During development, combinations of PSEDN TFs specify eye, kidney, and inner ear components. In cancer, where embryonic transcriptional programs are often

<sup>1</sup>Program in Virology, The Graduate School of Arts and Sciences, Harvard University, Cambridge, Massachusetts, USA; <sup>2</sup>Department of Medical Oncology, Dana-Farber Cancer Institute, Boston, Massachusetts, USA; <sup>3</sup>Experimental Therapeutics Core, Dana-Farber Cancer Institute, Boston, Massachusetts, USA; <sup>4</sup>Robert and Renée Belfer Center for Applied Cancer Science, Dana-Farber Cancer Institute, Boston, Massachusetts, USA; and <sup>5</sup>Department of Medicine, Brigham and Women's Hospital, Harvard Medical School, Boston, Massachusetts, USA

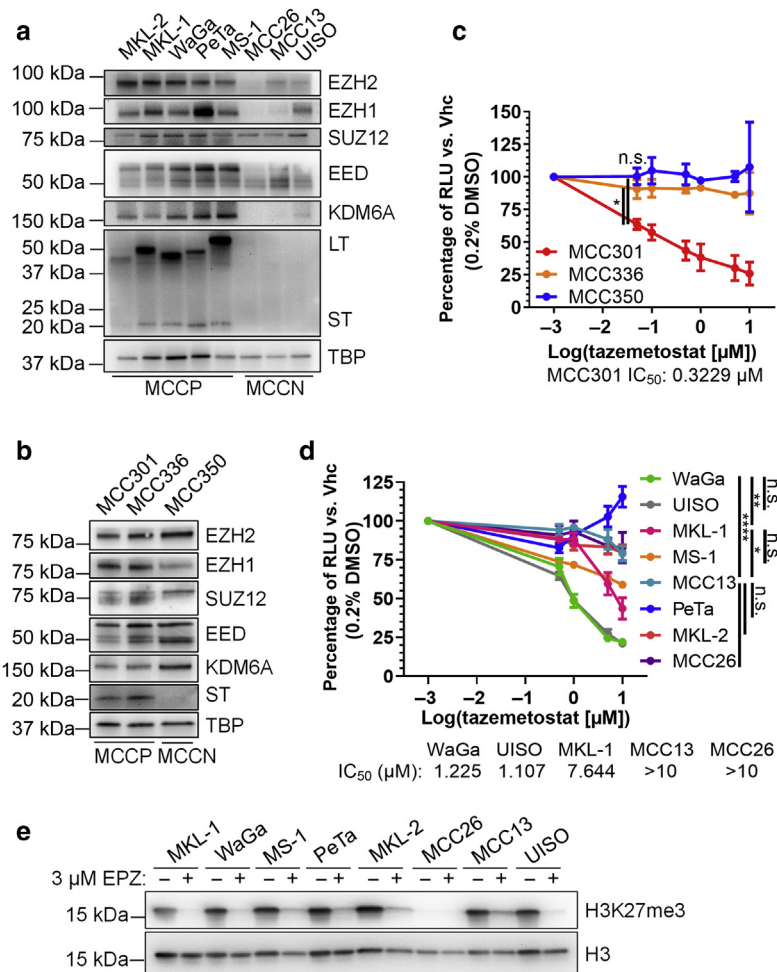
Correspondence: James A. DeCaprio, Department of Medical Oncology, Dana-Farber Cancer Institute, 450 Brookline Avenue, Mayer 440, Boston, Massachusetts 02215, USA. E-mail: james\_decaprio@dfci.harvard.edu

Abbreviations: DEG, differentially expressed gene; EZH2i, EZH2 inhibitor; H3K27me3, histone H3 lysine 27 trimethylation; H3K4me3, histone H3 lysine 4 trimethylation; MCC, Merkel cell carcinoma; PRC2, Polycomb repressive complex 2; PSEDN, PAX-SIX-EYA-DACH network; TF, transcription factor

Received 4 November 2021; revised 28 February 2022; accepted 7 March 2022; accepted manuscript published online XXX; corrected proof published online XXX

**Figure 1. MCC cell lines respond variably to tazemetostat, but this is not fully explainable by PRC2 component expression.** (a)

Immunoblots of established and (b) patient-derived cell lines. (a) is representative of three experiments; (b) of two. (c) Day 12 CellTiter-Glo assay of tazemetostat-treated patient-derived and (d) established cell lines. IC<sub>50</sub>s are shown for lines for which they are calculable. For (c), N = 2; mean ± SD; one-way ANOVA at 50 nM with Tukey's posthoc tests. For (d), N = 3; mean ± SEM; one-way ANOVA at 5 μM with Tukey's posthoc tests for selected comparisons; \**P* < 0.05, \*\**P* < 0.01, \*\*\*\**P* < 0.0001. (e) Immunoblots of histones from cells treated with 3 μM EPZ011989 for 6 days. Representative of three experiments. EPZ, EPZ011989; H3K27me3, histone H3 lysine 27 trimethylation; IC<sub>50</sub>, half-maximal inhibitory concentration; LT, Merkel cell polyomavirus large T antigen; MCC, Merkel cell carcinoma; MCCN, nonviral Merkel cell carcinoma; MCCP, viral Merkel cell carcinoma; n.s., nonsignificant; PRC2, Polycomb repressive complex 2; RLU, relative light unit; ST, Merkel cell polyomavirus small T antigen; vhc, vehicle; vs., versus.



recapitulated, SIX1 activates metastasis and cell cycle genes (Liu et al., 2016). Although PRC2 and the PSEDN crosstalk during development (Cohen et al., 2021; Delgado-Olguín et al., 2012; Liu et al., 2020; Yan et al., 2016), no studies have shown direct relationships between PRC2 and SIX in cancer. In this study, we uncover a requirement for EZH2-dependent repression of inner ear differentiation genes, particularly *SIX1*, in MCC. Our work identifies a potential therapeutic vulnerability and provides mechanistic insight into EZH2i-induced transcriptional perturbation in MCC.

## RESULTS

### PRC2 subunit expression in MCC cells and EZH2i sensitivity

We profiled expression of core PRC2 subunits and the opposing histone H3 lysine 27 demethylase KDM6A in established and patient-derived MCC cell lines (Figure 1a and b). All tested subunits were expressed in each line except MCC13 and MCC26. MCC13 had low EZH1, concordant with nonsense and missense mutations documented in DepMap (Ghandi et al., 2019). MCC26 had low EZH1/EZH2, although no mutations were noted. All viral MCC lines expressed KDM6A, with lower levels in established nonviral MCC lines.

The effect of 12-day tazemetostat treatment on cell viability was assessed using the CellTiter-Glo Luminescent Cell Viability Assay Kit (Promega, Madison, WI) (Figure 1c

and d). Responses segregated into high sensitivity (WaGa, UISO, and MCC301), intermediate sensitivity (MKL-1 and MS-1), and resistant (MKL-2, PeTa, MCC13, MCC26, MCC336, and MCC350) groups. MCC26 with low EZH1/EZH2 was resistant, but no patterns linking sensitivity and PRC2 subunit or KDM6A expression were apparent. Sensitivity was independent of p53 (Houben et al., 2013) and viral status, although more viral MCC lines were sensitive (4 of 7) than nonviral MCC lines (1 of 4). We compared the sensitivity of MKL-1 and WaGa with previously reported highly sensitive G401 (Knutson et al., 2013) and resistant A549 cells (Januario et al., 2017) and observed responses between these controls (Supplementary Figure S1a). To determine whether MCC tazemetostat responses reflected on-target sensitivity to PRC2 inhibition, we compared responses to the EED inhibitor EED226 (Qi et al., 2017). We observed tazemetostat-sensitive but not resistant lines exhibited sigmoidal EED226 inhibition curves (Supplementary Figure S1b).

To determine growth inhibition kinetics, proliferation assays were performed using two EZH2i (Supplementary Figure S2), tazemetostat (Knutson et al., 2013) and EPZ011989 (Campbell et al., 2015). Growth inhibition was not observed until day 9 and reached a cytotoxic threshold in this assay ~3 μM EPZ011989 in MKL-1, and 0.5 μM tazemetostat in WaGa. Accordingly, 3 μM EPZ011989 inhibited cell-cycle progression in MKL-1 but not in MCC13,

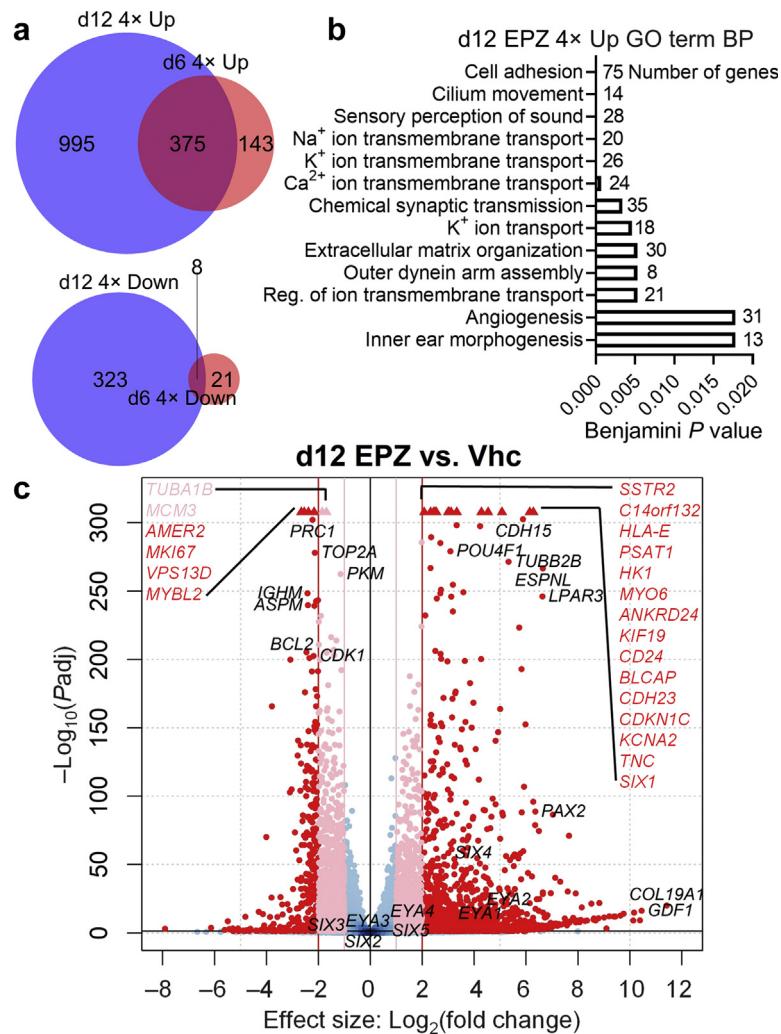


**Figure 2. RNA sequencing of EPZ011989-treated MKL-1 reveals early and late transcriptional effects with PSEDN transcription factor upregulation.** (a) Venn diagrams of significant four-fold upregulated and downregulated DEGs after 6- or 12-day treatment with 3  $\mu$ M EPZ011989. (b) GO term BP analysis of day 12 four-fold upregulated DEGs. (c) Volcano plot highlighting two-fold (pink) and four-fold (red) significantly upregulated and downregulated genes on day 12. Triangle indicates  $P_{adj} < 2.23E-308$ . adj, adjusted; BP, biological process; Ca<sup>2+</sup>, calcium; d, day; DEG, differentially expressed gene; down, downregulated; EPZ, EPZ011989; GO, Gene Ontology; K<sup>+</sup>, potassium; Na<sup>+</sup>, sodium; PSEDN, PAX-SIX-EYA-DACH network; reg., regulation; up, upregulated; vhc, vehicle; vs., versus.

beginning on day 6 and increasing by day 12 (Supplementary Figure S3). The molecular effects of tazemetostat/EPZ011989 after 6 days were assessed in MCC lines, G401, and A549 by immunoblotting H3K27me3 (Figure 1e, Supplementary Figure S1c). H3K27me3 was reduced in all lines except MCC26, consistent with reports that EZH2i-resistant cells still exhibit molecular responses (Hernando et al., 2016; Qadeer et al., 2019). H3K27me3 loss was also observed in EED226-treated MKL-1 (Supplementary Figure S1d).

#### EPZ011989-treated MCC cells exhibit PSEDN dysregulation

Transcriptional changes were profiled in MKL-1 treated with 3  $\mu$ M EPZ011989 for 6 and 12 days to assess responses before and after proliferation changes (Supplementary Figure S2a and S4a). We observed predominantly upregulated differentially expressed genes (DEGs) on day 6 (Figure 2a, Supplementary Figure S4b, and Supplementary Table S1) and both up- and downregulated DEGs on day 12 (Supplementary Table S2). This suggests that the day 6 DEGs reflected loss of repression of direct PRC2 targets, whereas the day 12 DEGs included indirect targets. Gene Ontology analyses of the day 6 and 12 upregulated DEGs were

enriched for terms related to ion transport, hearing, and cell adhesion (Figure 2b, Supplementary Figure S4c, Supplementary Table S3). Adhesion-related gene upregulation was consistent with increased clumping observed in EPZ011989/EED226-treated MKL-1 (Supplementary Figure S5). The day 12 downregulated DEGs featured cell cycle signatures (Supplementary Figure S4d) consistent with decreased proliferation. Epigenetic landscape in silico deletion analysis (Qin et al., 2020) was performed to predict DEG-regulating TFs (Supplementary Figure S4e and f). Targets of PRC2 subunits EZH2, SUZ12, and JARID2 were among the upregulated DEGs, whereas targets of cell-cycle regulators E2F1/4, MYBL2, and FOXM1 were among the day 12 downregulated DEGs.

The most significantly upregulated gene on both days was *SIX1*, a PSEDN TF involved in inner ear hair cell development, although upregulation was nonuniform across the PSEDN (Figure 2c and Supplementary Figure S6). The appearance of *MYO6*, a cochlear *SIX1* target gene (Li et al., 2020), as a top day 12 upregulated gene suggested *SIX1* could induce transcriptional changes in response to EPZ011989. This was supported by epigenetic landscape in

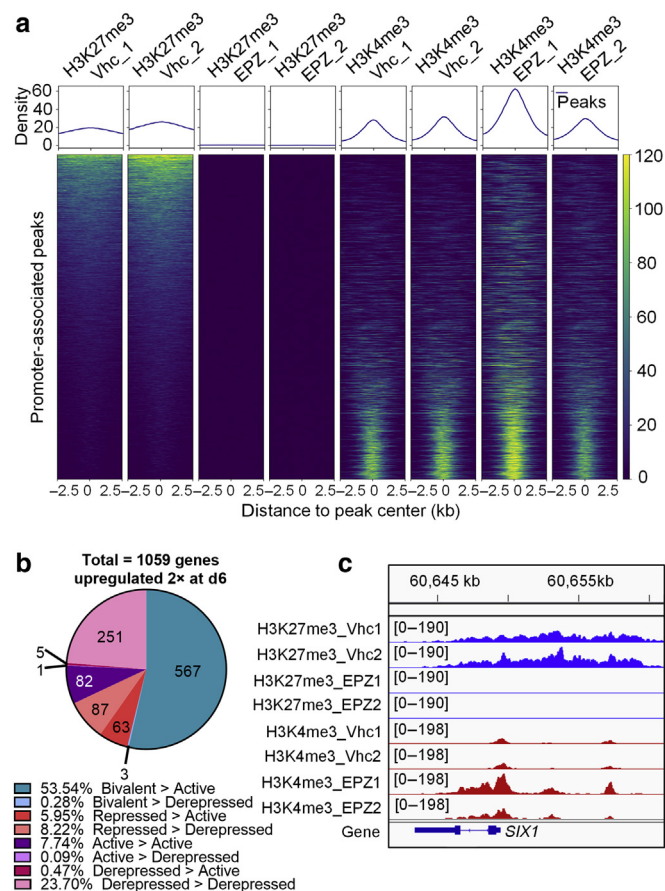


**Figure 3. CUT&RUN of EPZ011989-treated MKL-1 reveals most upregulated genes have bivalent promoters that lose H3K27me3 and retain H3K4me3 after treatment.** (a) Peak-centered heatmap of overlapping H3K27me3 and H3K4me3 peaks annotated to promoters in vehicle and the corresponding regions in samples treated with 3  $\mu$ M EPZ011989 for 6 days. (b) Promoter classifications of the 1,059 two-fold upregulated DEGs on day 6. Genes were classified according to presence or absence of promoter-associated peaks of each mark in the vehicle and EPZ011989 conditions, as shown in [Supplementary Table S9](#). (c) H3K27me3 and H3K4me3 peaks in the *SIX1* promoter region in vehicle and EPZ011989 conditions. d, day; EPZ, EPZ011989; H3K27me3, histone H3 lysine 27 trimethylation; H3K4me3, histone H3 lysine 4 trimethylation; kb, kilobase; vhc, vehicle.

silico deletion analysis showing targets of *SIX2*, which shares the *SIX1* binding motif (O'Brien et al., 2016), were among the day 12 upregulated DEGs ([Supplementary Figure S4f](#)). We confirmed these results by RT-qPCR ([Supplementary Figure S7](#)), testing hair cell *SIX1* targets (Li et al., 2020) and other hearing-related genes (Azaiez et al., 2018; Ebrahim et al., 2016). Immunoblots also confirmed EPZ011989 dose/time-dependent *SIX1* and hair cell protein expression changes in MKL-1 and WaGa ([Supplementary Figure S8](#)).

#### Most genes upregulated by EPZ011989 are bivalent at baseline

To identify direct PRC2 targets, CUT&RUN was performed for H3K27me3 and H3K4me3 after 6-day MKL-1 treatment with vehicle or 3  $\mu$ M EPZ011989. Nearly all H3K27me3 peaks in vehicle ([Supplementary Table S4](#)) were lost after treatment ([Supplementary Figure S9](#)), whereas H3K4me3

peaks were largely unaffected ([Supplementary Figure S10](#) and [Supplementary Table S5](#) and 6). Examining bivalent promoters ([Supplementary Figure S11](#)) with overlapping H3K27me3/H3K4me3 peaks in vehicle confirmed H3K27me3 was lost after treatment whereas H3K4me3 was mostly retained ([Figure 3a](#)). We generated a gene list with this bivalent to active signature ([Supplementary Table S7](#)) and performed Gene Ontology analyses ([Supplementary Table S8](#)). This revealed a TF signature, supporting the idea that EPZ011989 led to multiple waves of transcriptional changes, with early upregulated genes influencing later waves ([Supplementary Figure S12a](#) and b).

The RNA sequencing and CUT&RUN were integrated to identify genes (bivalent, repressed, active, or derepressed according to H3K27me3/H3K4me3 promoter peaks [[Supplementary Table S9](#)]) that were upregulated by EPZ011989 ([Supplementary Table S10](#)). Of the day 6 two-fold upregulated DEGs, 54% were bivalent in vehicle and became active when H3K27me3 was lost after treatment, including *SIX1* ([Figure 3b](#) and c). Among other PSEDN members, *SIX2/5/6*, *EYA2*, and *PAX2* were also direct PRC2 targets, although only *EYA2* and *PAX2* were upregulated ([Supplementary Figure S12c](#)). This is consistent with the model that H3K27me3 loss was insufficient to upregulate transcription without activating inputs reflected by H3K4me3. *SIX1* may be one such activator for some DEGs, including PRC2 targets like *GIPC3* and nontargets like *MYO6* ([Supplementary Figure S13](#)).

#### *SIX1*, *SIX2*, and *EYA4* are critical for tazemetostat sensitivity

To identify genes required for EZH2i sensitivity, a CRISPR-Cas9 knockout screen was performed using the genome-wide H3 library (a gift of Xiaole Shirley Liu and Myles Brown, 133914, Addgene, Watertown, MA) in MKL-1 treated with 1.5  $\mu$ M tazemetostat ( $\sim$ IC<sub>30</sub>) for 15 days to ensure 8–10 cell doublings ([Supplementary Figure S14a–e](#) and [Supplementary Table S11](#) and 12). Among the most positively selected genes after tazemetostat treatment versus vehicle were *SIX1*, *SIX2*, and *EYA4* ([Figure 4a](#) and [Supplementary Figure S14f](#)). Of the top 100 positively selected genes, 15 were PRC2 targets, including *SIX1* and *LRIG1*, which were also upregulated at least two-fold on day 6 ([Figure 4b](#) and [Supplementary Table S13](#)). Negatively selected genes included PRC1 and PRC2 components ([Supplementary Figure S14g](#)), consistent with reports that they cooperate (Van Mierlo et al., 2019).

To validate the screen, we generated MKL-1 polyclonal knockouts of *SIX1*, *SIX2*, or *EYA4* and observed that they became tazemetostat-resistant ([Figure 4c](#)). Immunoblots showed knockout was efficient and the targeted genes were coregulated ([Figure 4d](#)). This agrees with findings that *SIX1/2* are crossregulated (O'Brien et al., 2016) and EYAs stabilize *SIX1* (Patrick et al., 2009). All knockouts also dampened tazemetostat-induced PUMA activation. Although PUMA was activated, p53 levels remained stable, supporting the finding that p53 status was not predictive for tazemetostat sensitivity. Knockout also dampened post-treatment morphological changes, suggesting that they resulted from PSEDN activity ([Supplementary Figure S15](#)).

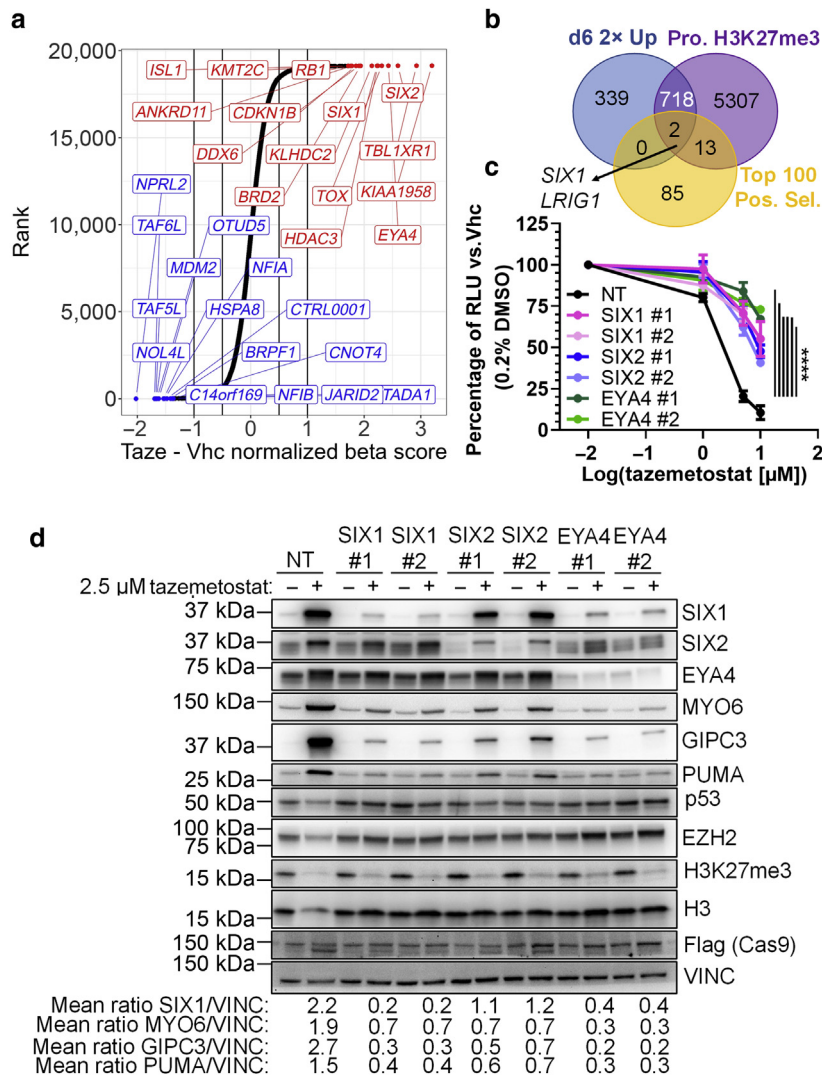


**Figure 4. CRISPR-Cas9 knockout screen shows *SIX1*, *SIX2*, or *EYA4* knockout renders MKL-1 resistant to tazemetostat.** (a) Cell cycle normalized beta score differences between screen conditions. Red—top positively selected genes. Blue—top negatively selected. (b) Venn diagram comparing day 6 two-fold upregulated DEGs, genes with promoter-associated H3K27me3, and the top 100 positively selected genes from the screen. (c) 15-day CellTiter-Glo assay of tazemetostat-treated MKL-1 polyclonal knockouts generated with guide pairs targeting indicated genes or a NT pair. N = 3; mean ± SEM; two-way ANOVA with Dunnett posthoc tests; \*\*\*\*P < 0.0001 each line versus NT at 5 μM; all also significant at 10 μM. (d) Day 15 immunoblots of polyclonal knockout MKL-1 treated with vehicle or 2.5 μM tazemetostat. Mean densitometric ratio of bands versus VINC calculated using ImageJ (National Institutes of Health, Bethesda, MD) for tazemetostat-treated samples. N = 3. #, guide pair number; d, day; DEG, differentially expressed gene; H3K27me3, histone H3 lysine 27 trimethylation; NT, nontargeting; pos. sel., positively selected; pro., promoter; RLU, relative light unit; taze, tazemetostat; up, upregulated; vhc, vehicle; vs., versus.

### SIX1 transcriptional activity is critical for tazemetostat-dependent and -independent viability loss

We suspected SIX1 transcriptional activity was important for tazemetostat sensitivity. Expression of SIX1 increased MKL-1 sensitivity (Figure 5a and b). However, expression of transcriptionally-impaired SIX1 mutants—V17E is defective for EYA binding (Patrick et al., 2013) and ΔE133 for DNA binding (Patrick et al., 2009)—did not. It is unclear whether these mutants are hypomorphic or act as dominant negatives by competing for DNA binding sites and EYAs, respectively (Shah et al., 2020). However, only SIX1 ΔE133 enhanced resistance, suggesting that it may be dominant negative in these cells.

We asked whether increased SIX1 alone could reduce cell viability in MCC lines. MKL-1 expressing wild-type SIX1 or ΔE133 experienced significant viability decrease after 9 days of induction (Figure 5c). The induction time needed to affect cell viability was similar to the maximal time SIX1 would be derepressed during 12-day EZH2i treatment (Supplementary Figure S8a), and to the time needed for EZH2i-induced growth inhibition (Supplementary Figure S2). This supports the finding that SIX1 activity was critical for EZH2i responses. The effect of the likely dominant negative ΔE133 suggests

MKL-1 required at least some minimal SIX1/EYA activity for survival. This agrees with the CRISPR screen showing positive selection of *SIX1*, *SIX2*, and *EYA4* knockout with tazemetostat but negative selection with vehicle (Supplementary Figure S14f). In contrast to MKL-1, SIX1 induction in MCC13 neither reduced viability (Figure 5c) nor upregulated MYO6/GIPC3 (Supplementary Figure S16a), suggesting that SIX1 activity was impaired or SIX1 had different targets than in MKL-1.

We then asked whether SIX1 upregulation after EZH2i treatment occurred across MCC lines. Each was treated with 3 μM EPZ011989 for 6 days and immunoblotted for SIX1, MYO6, and GIPC3 (Figure 5d). Except for UIISO, each sensitive line (MKL-1, WaGa, MS-1, and MCC301) upregulated SIX1 and at least one downstream target (Figure 5e). By contrast, UIISO and the resistant lines (MKL-2, PeTa, MCC26, and MCC13) experienced minimal SIX1 upregulation. Notably, MKL-1 also upregulated SIX1, MYO6, and GIPC3 after 5 μM EED226 treatment, which is consistent with SIX1 derepression through on-target PRC2 inhibition (Supplementary Figure S16b). Neither baseline SIX1 levels (Supplementary Figure S16c and d) nor EYA profiles

**Figure 5. SIX1 transcriptional activity is essential for tazemetostat-dependent and -independent cell viability loss, and SIX1 derepression correlates with EZH2 inhibitor sensitivity.** (a) Day 12 CellTiter-Glo assay of tazemetostat-treated MKL-1 expressing GFP or SIX1. N = 3; mean  $\pm$  SEM; two-way ANOVA with Dunnett posthoc tests; \* $P$  < 0.05, \*\* $P$  < 0.01, \*\*\*\* $P$  < 0.0001 versus GFP; V17E n.s. (b) Control immunoblots of vehicle-treated cells induced alongside a. SIX1 hi panel shows higher exposure to highlight baseline SIX1 expression in GFP control. Representative of three experiments. (c) Day 6 and day 9 CellTiter-Glo assays of MKL-1 and MCC13 expressing GFP or SIX1. N = 3; mean  $\pm$  SEM; two-way repeated measures ANOVAs for each parental line with Dunnett posthoc tests; \* $P$  < 0.05. (d) Immunoblots of established MCC lines and (e) MCC301 cells treated with vehicle or 3  $\mu$ M EPZ011989 for 6 days. Representative of three experiments; EYA1/EYA2 representative of two. Mean densitometric ratio versus TBP calculated with ImageJ. N = 3.

\*EZH2i sensitivity, d, day; dox, doxycycline; EPZ, EPZ011989; n.s., nonsignificant; RLU, relative light unit; vhc, vehicle; vs., versus.

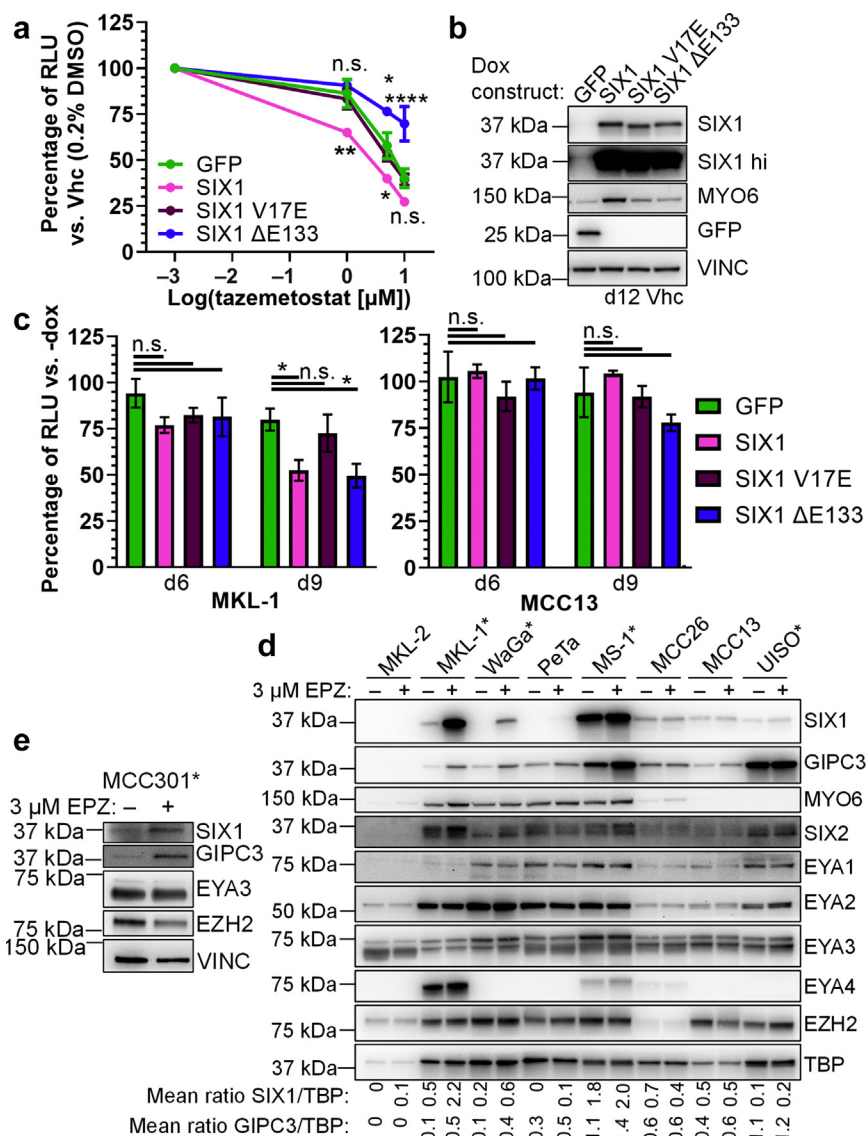


(Figure 5d) were predictive of EZH2i sensitivity, and SIX1 upregulation was an MCC-specific sensitivity correlate (Supplementary Figure S16d).

### Tazemetostat delays MCC xenograft growth and derepresses SIX1 in vivo

To test tazemetostat efficacy in vivo, MKL-1 xenografts were grown in NOD *scid* gamma mice and treated with vehicle or 400 mg/kg tazemetostat two times a day. This was well tolerated (Supplementary Figure S17a) and was similar to maximal twice daily dosing reported previously (Januario et al., 2017; Knutson et al., 2014, 2013). Tazemetostat had a delayed effect on tumor growth with a significant difference in volume between treatment arms evident by day 19 (Figure 6a and b). Least-squares nonlinear regression was used to fit mean models for both treatment arms through the end of treatment that described the curves significantly better than one equation (Figure 6c and Supplementary Figure S17b–d). Tazemetostat-treated mice trended toward increased survival (Figure 6d), with none reaching endpoint

tumor volume (2,000 mm<sup>3</sup>) until day 22 and 3 of 9 surviving after day 26, by which time all vehicle-treated mice reached endpoint. Before day 22, 3 of 9 tazemetostat-treated mice were killed owing to tumor ulceration, which was not observed in the vehicle arm. One tazemetostat-treated mouse experienced tumor regression from days 19–26. On day 33, treatment was withdrawn and endpoint reached on day 50.

Pairs of vehicle- and tazemetostat-treated tumors collected on the same day were compared by immunoblot (Figure 6e). All 3 of 3 tazemetostat-treated tumors that were examined exhibited H3K27me3 loss. SIX1 induction occurred in 3 of 3 and MYO6 induction in 2 of 3. A tazemetostat-treated tumor collected on day 33 was compared with the day 50 regrown tumor. Although H3K27me3 levels were restored, SIX1/MYO6 remained elevated 17 days after treatment removal, suggesting tumor adaptation to SIX1 activity.

### DISCUSSION

EZH2 overexpression sensitizes several neuroendocrine cancers to EZH2i and has been reported in MCC (Harms

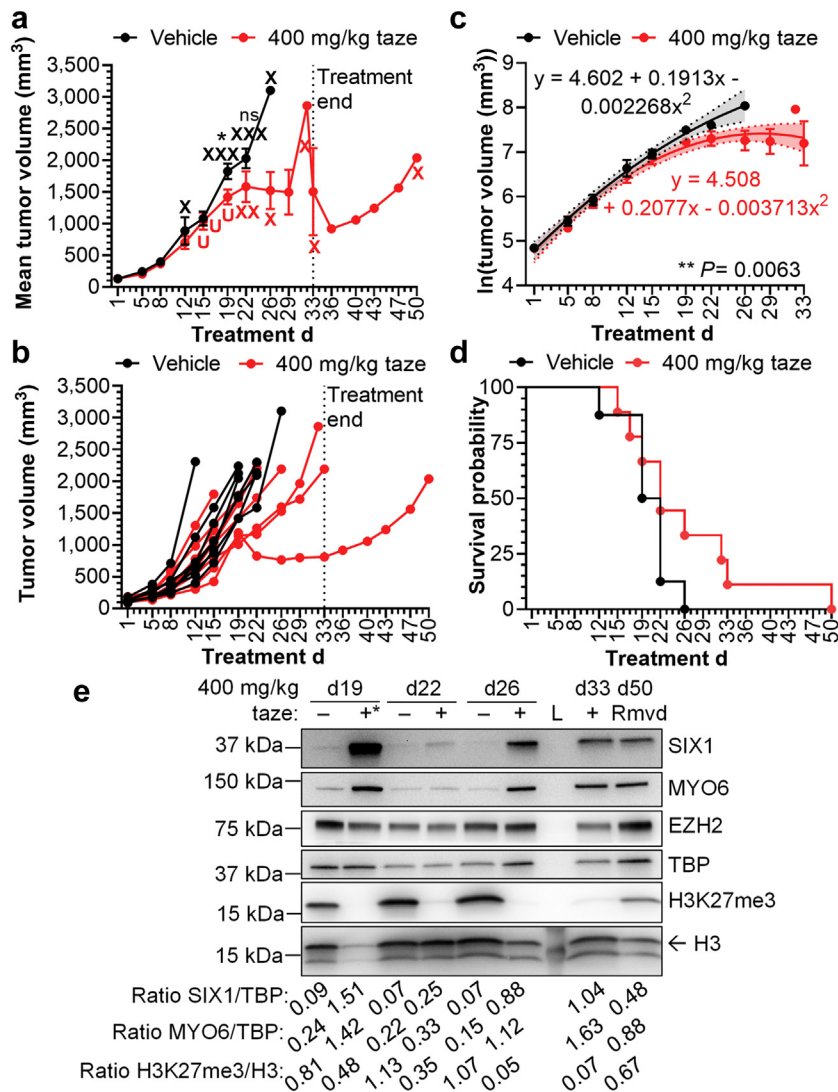


**Figure 6. Tazemetostat delays growth of MKL-1 xenografts and induces global loss of H3K27me3 with SIX1 and MYO6 expression.** (a) Tumor volume measurements by treatment arm. Mean ± SEM; N = 8 (vehicle) or 9 (tazemetostat); days 19 and 22 two-sided *t*-tests; \**P* < 0.05. One mouse measured early on day 32 owing to tumor burden concerns. X indicates mouse killed because of volume endpoint (2,000 mm<sup>3</sup>); U because of ulceration. (b) Individual measurements. (c) Least-squares nonlinear regression of ln-transformed volumes. Mean ± SEM. Shading indicates 95% confidence interval. Extra sum-of-squares F test. (d) Survival curves. Mantel-Cox test; *P* = 0.1526. (e) Immunoblots of vehicle- and tazemetostat-treated tumor pairs harvested on days 19, 22, and 26; and immunoblots comparing tazemetostat-treated tumors harvested on day 33 and on day 50 after treatment withdrawal. \*Tumor ulceration. L—ladder. Densitometric ratio of bands versus TBP or H3 calculated with ImageJ. d, day; H3K27me3, histone H3 lysine 27 trimethylation; rmvd, day 33 treatment removal; taze, tazemetostat.

et al., 2017; Veija et al., 2017). MCC shares similarities with normal skin Merkel cells (Leonard et al., 2002; Tang and Toker, 1978), whose expansion is restricted by PRC2-dependent repression (Bardot et al., 2013; Perdigoto et al., 2016) of the mechanosensory- and MCC-associated TFs SOX2 and ATOH1 (Cheng et al., 2017). These data suggest PRC2 may be an epigenetic vulnerability in MCC, and we characterized the response to EZH2i in MCC cell lines and xenografts.

Three independent analyses—RNA sequencing, CUT&RUN, and CRISPR screening—using two EZH2i identified SIX1 as a PRC2 target in MCC cells that was critical for EZH2i sensitivity. Early SIX1 upregulation correlated with later EZH2i-induced viability loss in multiple MCC lines and in vivo activity. Although most previous studies found that SIX1 is protumorigenic (Coletta et al., 2004; Li et al., 2018, 2013a, 2013b; Zhou et al., 2020), at least one found a protective effect in endometrial cells (Suen et al., 2019). In this study, we showed growth inhibitory SIX1 activity in MCC.

We observed that loss of epigenetic repression was insufficient to upregulate any particular gene. Positive inputs,

reflected by activating H3K4me3, were also required. Previous work indicates SIX1 is transcriptionally regulated by SIX, PAX, SOX, and E-box-binding proteins (Sato et al., 2012), including ATOH1, which we previously found bound upstream of SIX1 (Park et al., 2020). We and others have observed that virus-positivity correlates with higher expression of ATOH1/SOX2 in MCC (Supplementary Figure S18a) (Gravemeyer et al., 2021; Park et al., 2020). Lower expression of positive regulators like ATOH1/SOX2 may partly explain why EPZ011989-treated MCC13 and UISO did not upregulate SIX1. Understanding what other factors determine whether EZH2i upregulates SIX1 in a given MCC line will be fruitful for future study.

Higher levels of the mechanosensory TFs ATOH1, SOX2, and POU4F3 (Supplementary Figure S18b) may also prime the MCC transcriptional landscape to upregulate inner ear hair cell genes after SIX1 derepression. Yu et al. (2021) showed that >50% of POU4F3-dependent, ATOH1-bound open enhancers in hair cells are also accessible in Merkel cells, but SIX motifs are only enriched in hair cell-specific enhancers. Given the similarities between Merkel cells and

MCC, *SIX1* derepression in MCC may induce an aberrant hair cell differentiation program resulting in cell cycle suppression. Lower ATOH1/SOX2 levels could explain why MCC13 resisted *SIX1*-induced viability loss and *SIX1* target upregulation. More broadly, it is likely that PRC2-dependent *SIX1* repression in epidermal progenitors (Cohen et al., 2021, 2018) prevents activation of a hair cell program and promotes correct Merkel cell differentiation.

In summary, we have unveiled a potential therapeutic vulnerability in a subset of MCC cell lines. The efficacy of prolonged single-agent tazemetostat treatment in the MKL-1 xenografts is similar to that observed by Gardner et al. (2017) for EPZ011989 in small cell lung cancer patient-derived xenografts. Because they found greater efficacy in EZH2i-based combination therapy, we suggest investigation of EZH2i in MCC in combination with immune checkpoint blockade (Burr et al., 2019) or other epigenetic therapies (Huang et al., 2018). Two of our findings will be relevant in further study of MCC and other cancers: (i) bivalent TFs are among the most significant EZH2i targets, and (ii) these direct targets are required to observe full EZH2i effects, likely because they drive secondary waves of growth inhibitory gene expression.

## MATERIALS AND METHODS

### Tissue culture

Established MCC and A549 lines were cultured in RPMI-1640, and 293T in DMEM, plus GlutaMAX (Thermo Fisher Scientific, Waltham, MA) and 10% fetal bovine serum (MilliporeSigma, Burlington, MA). G401 were cultured in McCoy's 5A modified medium plus penicillin/streptomycin (Thermo Fisher Scientific) and 10% fetal bovine serum. Patient-derived lines were cultured in Neurocult NS-A medium plus 10% NS-A supplement, 20 ng/ml fibroblast growth factor, 0.0002% heparin (Stemcell Technologies, Vancouver, Canada), 20 ng/ml epidermal growth factor (Thermo Fisher Scientific), and penicillin/streptomycin. Validation/cell line generation are described in Supplementary Materials and Methods.

### CellTiter-Glo assays

MKL-1, MKL-2, MS-1, MCC301, MCC336, and MCC350 were initially Accutase-treated (Stemcell Technologies). Cells were plated with 0.2% DMSO, tazemetostat, or EED226 (Cayman Chemical, Ann Arbor, MI). Inducible lines were treated with 1.5 µg/ml doxycycline (GoldBio Technology, St. Louis, MO). Every 3 days, each line was split according to its vehicle condition's needs with inhibitor/doxycycline refreshment. Cells were lysed with CellTiter-Glo.

### Immunoblot

Cells were lysed in radioimmunoprecipitation assay buffer except for histone extraction, where the Abcam protocol was used (<https://www.abcam.com/protocols/histone-extraction-protocol-for-western-blot>). Lysates were run in an SDS-PAGE gel, transferred to polyvinylidene difluoride membrane, blocked in 5% milk, incubated at 4 °C overnight in primary antibody (Supplementary Table S14; Ab5 described in Cheng et al., 2017; Rodig et al., 2012), and imaged with SuperSignal West Femto substrate (Thermo Fisher Scientific).

### RNA sequencing

MKL-1 were treated in triplicate with 1% ethanol or 3 µM EPZ011989 (Cayman Chemical) for 6 and 12 days with refreshment every 3 days. RNA was TRIzol (Thermo Fisher Scientific)/chloroform

extracted. Sequencing/analysis are described in Supplementary Materials and Methods.

### CUT&RUN

MKL-1 were treated in duplicate with 1% ethanol or 3 µM EPZ011989 for 6 days with day 3 refreshment. CUT&RUN was performed as described previously with samples split into thirds for antibody binding (Janssens and Henikoff, 2019; Meers et al., 2019). Accutase-treated cells ( $4 \times 10^5$ ) were permeabilized with 0.025% digitonin and incubated overnight at 4 °C with antibody (Supplementary Table S14). pA-MNase (1:2,000; from Stuart Orkin, Dana-Farber Cancer Institute, Boston, MA) was added. Stop buffer included 200 pg/ml *E. coli* spike-in DNA (EpiCypher, Durham, NC). DNA was phenol/chloroform extracted. Sequencing/analysis are described in Supplementary Materials and Methods.

### CRISPR-Cas9 screen

The H3 CRISPR-Cas9 library suspension cell protocol (<https://www.addgene.org/pooled-library/liu-crispr-knockout-h3/>) was used with modifications. Accutase-treated MKL-1 cells ( $1 \times 10^8$ ) were spin-infected with viral supernatant sufficient for 30% survival after selection. After selection,  $3 \times 10^7$  Accutase-treated cells were plated at  $5 \times 10^5$ /ml cell density and treated with 0.2% DMSO or 1.5 µM tazemetostat, and  $5 \times 10^7$  were harvested. Cells were replated at  $5 \times 10^5$ /ml cell density every 3 days. DNA was phenol/chloroform extracted. Guides were amplified using the custom protocol (primers are mentioned in Supplementary Table S15) with Q5 polymerase (New England Biolabs, Ipswich, MA). Spinefection and sequencing/analysis are described in Supplementary Materials and Methods.

### Xenografts

The Dana-Farber Cancer Institute Experimental Therapeutics Core performed the xenograft study. This study was approved by the Dana-Farber Cancer Institute Institutional Animal Care and Use Committee and is compliant with the National Institutes of Health Guide for the Care and Use of Laboratory Animals. The 13-week-old female NOD *scid* gamma mice (The Jackson Laboratory, Bar Harbor, ME) were implanted subcutaneously with  $5 \times 10^6$  MKL-1 cells in 100 µL PBS with 50% matrigel. Tumors grew to a range of 91.9–188.5 mm<sup>3</sup> before treatment randomization. Nine mice were treated with 400 mg/kg tazemetostat (MedChemExpress, Monmouth Junction, NJ) and 8 with vehicle (0.5% methylcellulose with 0.1% Tween 80 in sterile water; pH adjusted to 4.0 with 1N hydrochloride) two times a day by oral gavage. Tumor volume was measured twice weekly until tumors reached endpoint volume (2,000 mm<sup>3</sup>) or became ulcerated, when mice were killed. Tumors were flash frozen in liquid nitrogen. For immunoblotting, frozen tumors were ground with mortar and pestle and disrupted in radioimmunoprecipitation assay buffer with the Qiagen TissueRuptor II (Qiagen, Hilden, Germany).

### Data availability statement

Datasets related to this article can be found at <https://www.ncbi.nlm.nih.gov/geo/query/acc.cgi?acc=GSE186899>, hosted at Gene Expression Omnibus (Edgar et al., 2002).

### ORCIDs

Ashley K. Gartin: <http://orcid.org/0000-0001-8072-6650>  
 Thomas C. Frost: <http://orcid.org/0000-0002-7855-1000>  
 Camille H. Cushman: <http://orcid.org/0000-0002-8792-661X>  
 Brittaney A. Leeper: <http://orcid.org/0000-0001-8807-2954>  
 Prafulla C. Gokhale: <http://orcid.org/0000-0002-1974-5921>  
 James A. DeCaprio: <http://orcid.org/0000-0002-0896-167X>

**CONFLICT OF INTEREST**

JAD has received support from Rain Therapeutics. Rain Therapeutics had no role in this study. The remaining authors state no conflict of interest.

**ACKNOWLEDGMENTS**

We thank Varsha Ananthapadmanabhan for methodological advice. We thank the Dana-Farber Cancer Institute Molecular Biology Core Facilities and Experimental Therapeutics Core. CHC was funded in part by a Ruth L. Kirschstein Predoctoral Individual National Research Service Award (F31CA239345).

**AUTHOR CONTRIBUTIONS**

Conceptualization: JAD; Formal Analysis: AKG, TCF, CHC; Funding Acquisition: JAD; Investigation: AKG, TCF, BAL; Methodology: CHC; Project Administration: PCG, JAD; Writing - Original Draft Preparation: AKG; Writing - Review and Editing: AKG, TCF, JAD.

**SUPPLEMENTARY MATERIAL**

Supplementary material is linked to the online version of the paper at [www.jidonline.org](http://www.jidonline.org), and at <https://doi.org/10.1016/j.jid.2022.03.008>.

**REFERENCES**

- Azaiez H, Booth KT, Ephraim SS, Crone B, Black-Ziegelbein EA, Marini RJ, et al. Genomic landscape and mutational signatures of deafness-associated genes. *Am J Hum Genet* 2018;103:484–97.
- Bardot ES, Valdes VJ, Zhang J, Perdigoto CN, Nicolis S, Hearn SA, et al. Polycomb subunits Ezh1 and Ezh2 regulate the Merkel cell differentiation program in skin stem cells. *EMBO J* 2013;32:1990–2000.
- Bernstein BE, Mikkelsen TS, Xie X, Kamal M, Huebert DJ, Cuff J, et al. A bivalent chromatin structure marks key developmental genes in embryonic stem cells. *Cell* 2006;125:315–26.
- Blanco E, González-Ramírez M, Alcaine-Colet A, Aranda S, Di Croce L. The bivalent genome: characterization, structure, and regulation. *Trends Genet* 2020;36:118–31.
- Burr ML, Sparbier CE, Chan KL, Chan YC, Kersbergen A, Lam EYN, et al. An evolutionarily conserved function of polycomb silences the MHC class I antigen presentation pathway and enables immune evasion in cancer. *Cancer Cell* 2019;36:385–401.e8.
- Byers LA, Wang J, Nilsson MB, Fujimoto J, Saintigny P, Yordy J, et al. Proteomic profiling identifies dysregulated pathways in small cell lung cancer and novel therapeutic targets including PARP1. *Cancer Discov* 2012;2:798–811.
- Campbell JE, Kuntz KW, Knutson SK, Warholc NM, Keilhack H, Wigle TJ, et al. EPZ011989, a potent, orally-available EZH2 inhibitor with robust in vivo activity. *ACS Med Chem Lett* 2015;6:491–5.
- Cheng J, Park DE, Berrios C, White EA, Arora R, Yoon R, et al. Merkel cell polyomavirus recruits MYC to the EP400 complex to promote oncogenesis. *PLoS Pathog* 2017;13:e1006668.
- Cohen I, Bar C, Liu H, Valdes VJ, Zhao D, Galbo PM Jr, et al. Polycomb complexes redundantly maintain epidermal stem cell identity during development. *Genes Dev* 2021;35:354–66.
- Cohen I, Zhao D, Bar C, Valdes VJ, Dauber-Decker KL, Nguyen MB, et al. PRC1 fine-tunes gene repression and activation to safeguard skin development and stem cell specification. *Cell Stem Cell* 2018;22:726–39.e7.
- Coletta RD, Christensen K, Reichenberger KJ, Lamb J, Micomono D, Huang L, et al. The Six1 homeoprotein stimulates tumorigenesis by reactivation of cyclin A1. *Proc Natl Acad Sci USA* 2004;101:6478–83.
- Dardenne E, Beltran H, Benelli M, Gayvert K, Berger A, Puca L, et al. N-Myc induces an EZH2-mediated transcriptional program driving neuroendocrine prostate cancer. *Cancer Cell* 2016;30:563–77.
- Delgado-Olguín P, Huang Y, Li X, Christodoulou D, Seidman CE, Seidman JG, et al. Epigenetic repression of cardiac progenitor gene expression by Ezh2 is required for postnatal cardiac homeostasis. *Nat Genet* 2012;44:343–7.
- Ebrahim S, Avenarius MR, Grati M, Krey JF, Windsor AM, Sousa AD, et al. Stereocilia-staircase spacing is influenced by myosin III motors and their cargos espin-1 and espin-like. *Nat Commun* 2016;7:10833.
- Edgar R, Domrachev M, Lash AE. Gene Expression Omnibus: NCBI gene expression and hybridization array data repository. *Nucleic Acids Res* 2002;30:207–10.
- Gardner EE, Lok BH, Schneeberger VE, Desmeules P, Miles LA, Arnold PK, et al. Chemosensitive relapse in small cell lung cancer proceeds through an EZH2-SLFN11 axis. *Cancer Cell* 2017;31:286–99.
- Ghandi M, Huang FW, Jané-Valbuena J, Kryukov GV, Lo CC, McDonald ER 3<sup>rd</sup>, et al. Next-generation characterization of the Cancer Cell Line Encyclopedia. *Nature* 2019;569:503–8.
- Gravemeyer J, Lange A, Ritter C, Spassova I, Song L, Picard D, et al. Classical and variant Merkel cell carcinoma cell lines display different degrees of neuroendocrine differentiation and epithelial-mesenchymal transition. *J Invest Dermatol* 2021;141:1675–86.e4.
- Harms KL, Chubb H, Zhao L, Fullen DR, Bichakjian CK, Johnson TM, et al. Increased expression of EZH2 in Merkel cell carcinoma is associated with disease progression and poorer prognosis. *Hum Pathol* 2017;67:78–84.
- Hernando H, Gelato KA, Lesche R, Beckmann G, Koehr S, Otto S, et al. EZH2 inhibition blocks multiple myeloma cell growth through upregulation of epithelial tumor suppressor genes. *Mol Cancer Ther* 2016;15:287–98.
- Hesbacher S, Pfitzer L, Wiedorfer K, Angermeyer S, Borst A, Haferkamp S, et al. RB1 is the crucial target of the Merkel cell polyomavirus large T antigen in Merkel cell carcinoma cells. *Oncotarget* 2016;7:32956–68.
- Houben R, Dreher C, Angermeyer S, Borst A, Utikal J, Haferkamp S, et al. Mechanisms of p53 restriction in Merkel cell carcinoma cells are independent of the Merkel cell polyoma virus T antigens. *J Invest Dermatol* 2013;133:2453–60.
- Huang X, Yan J, Zhang M, Wang Y, Chen Y, Fu X, et al. Targeting epigenetic crosstalk as a therapeutic strategy for EZH2-aberrant solid tumors. *Cell* 2018;175:186–99.e19.
- Italiano A, Soria JC, Toulmonde M, Michot JM, Lucchesi C, Varga A, et al. Tazemetostat, an EZH2 inhibitor, in relapsed or refractory B-cell non-Hodgkin lymphoma and advanced solid tumours: a first-in-human, open-label, phase 1 study. *Lancet Oncol* 2018;19:649–59.
- Janssens D, Henikoff S. CUT&RUN: targeted in situ genome-wide profiling with high efficiency for low cell numbers V3. <https://dx.doi.org/10.17504/protocols.io.zcpf2vn>; 2019. (accessed April 19, 2021).
- Januario T, Ye X, Bainer R, Alicke B, Smith T, Haley B, et al. PRC2-mediated repression of SMARCA2 predicts EZH2 inhibitor activity in SWI/SNF mutant tumors. *Proc Natl Acad Sci USA* 2017;114:12249–54.
- Knutson SK, Kawano S, Minoshima Y, Warholc NM, Huang KC, Xiao Y, et al. Selective inhibition of EZH2 by EPZ-6438 leads to potent antitumor activity in EZH2-mutant non-Hodgkin lymphoma. *Mol Cancer Ther* 2014;13:842–54.
- Knutson SK, Warholc NM, Wigle TJ, Klaus CR, Allain CJ, Raimondi A, et al. Durable tumor regression in genetically altered malignant rhabdoid tumors by inhibition of methyltransferase EZH2. *Proc Natl Acad Sci USA* 2013;110:7922–7.
- Kruger RG, Graves AP, McCabe MT. Activating mutations of the EZH2 histone methyltransferase in cancer. In: Pirrotta V, editor. Polycomb group proteins. Cambridge, MA: Academic Press; 2017. p. 259–88.
- Leindecker L, Jung PS, Krecioch I, Neumann T, Schleiffer A, Mechtler K, et al. LSD1 inhibition induces differentiation and cell death in Merkel cell carcinoma. *EMBO Mol Med* 2020;12:e12525.
- Leonard JH, Cook AL, Van Gele M, Boyle GM, Inglis KJ, Speleman F, et al. Proneural and proneuroendocrine transcription factor expression in cutaneous mechanoreceptor (Merkel) cells and Merkel cell carcinoma [published correction appears in *Int J Cancer* 2004;112:1086] *Int J Cancer* 2002;101:103–10.
- Li J, Zhang T, Ramakrishnan A, Fritzsche B, Xu J, Wong EYM, et al. Dynamic changes in cis-regulatory occupancy by Six1 and its cooperative interactions with distinct cofactors drive lineage-specific gene expression programs during progressive differentiation of the auditory sensory epithelium. *Nucleic Acids Res* 2020;48:2880–96.
- Li L, Liang Y, Kang L, Liu Y, Gao S, Chen S, et al. Transcriptional regulation of the Warburg effect in cancer by SIX1. *Cancer Cell* 2018;33:368–85.e7.
- Li Z, Tian T, Hu X, Zhang X, Nan F, Chang Y, et al. Six1 mediates resistance to paclitaxel in breast cancer cells. *Biochem Biophys Res Commun* 2013a;441:538–43.
- Li Z, Tian T, Lv F, Chang Y, Wang X, Zhang L, et al. Six1 promotes proliferation of pancreatic cancer cells via upregulation of cyclin D1 expression. *PLoS One* 2013b;8:e59203.
- Liu H, Hilliard S, Kelly E, Chen CH, Saifudeen Z, El-Dahr SS. The polycomb proteins EZH1 and EZH2 co-regulate chromatin accessibility and nephron progenitor cell lifespan in mice. *J Biol Chem* 2020;295:11542–58.

- Liu Y, Han N, Zhou S, Zhou R, Yuan X, Xu H, et al. The DACH/EYA/SIX gene network and its role in tumor initiation and progression. *Int J Cancer* 2016;138:1067–75.
- McCabe MT, Ott HM, Ganji G, Korenchuk S, Thompson C, Van Aller GS, et al. EZH2 inhibition as a therapeutic strategy for lymphoma with EZH2-activating mutations. *Nature* 2012;492:108–12.
- Meers MP, Bryson TD, Henikoff JG, Henikoff S. Improved CUT&RUN chromatin profiling tools. *Elife* 2019;8:e46314.
- O'Brien LL, Guo Q, Lee YJ, Tran T, Benazet JD, Whitney PH, et al. Differential regulation of mouse and human nephron progenitors by the Six family of transcriptional regulators. *Development* 2016;143:595–608.
- Park DE, Cheng J, Berrios C, Montero J, Cortés-Cros M, Ferretti S, et al. Dual inhibition of MDM2 and MDM4 in virus-positive Merkel cell carcinoma enhances the p53 response. *Proc Natl Acad Sci USA* 2019;116:1027–32.
- Park DE, Cheng J, McGrath JP, Lim MY, Cushman C, Swanson SK, et al. Merkel cell polyomavirus activates LSD1-mediated blockade of non-canonical BAF to regulate transformation and tumorigenesis [published correction appears in *Nat Cell Biol* 2020;22:752] *Nat Cell Biol* 2020;22:603–15.
- Patrick AN, Cabrera JH, Smith AL, Chen XS, Ford HL, Zhao R. Structure-function analyses of the human SIX1-EYA2 complex reveal insights into metastasis and BOR syndrome. *Nat Struct Mol Biol* 2013;20:447–53.
- Patrick AN, Schiemann BJ, Yang K, Zhao R, Ford HL. Biochemical and functional characterization of six SIX1 branchio-oto-renal syndrome mutations. *J Biol Chem* 2009;284:20781–90.
- Perdigoto CN, Dauber KL, Bar C, Tsai PC, Valdes VJ, Cohen I, et al. Polycomb-mediated repression and sonic hedgehog signaling interact to regulate Merkel cell specification during skin development. *PLoS Genet* 2016;12:e1006151.
- Qadeer ZA, Valle-Garcia D, Hasson D, Sun Z, Cook A, Nguyen C, et al. ATRX in-frame fusion neuroblastoma is sensitive to EZH2 inhibition via modulation of neuronal gene signatures. *Cancer Cell* 2019;36:512–27.e9.
- Qi W, Zhao K, Gu J, Huang Y, Wang Y, Zhang H, et al. An allosteric PRC2 inhibitor targeting the H3K27me3 binding pocket of EED. *Nat Chem Biol* 2017;13:381–8.
- Qin Q, Fan J, Zheng R, Wan C, Mei S, Wu Q, et al. Lisa: inferring transcriptional regulators through integrative modeling of public chromatin accessibility and ChIP-seq data. *Genome Biol* 2020;21:32.
- Ritter C, Fan K, Paschen A, Hardrup SR, Ferrone S, Nghiem P, et al. Epigenetic priming restores the HLA class-I antigen processing machinery expression in Merkel cell carcinoma. *Sci Rep* 2017;7:2290.
- Rodrig SJ, Cheng J, Wardzala J, DoRosario A, Scanlon JJ, Laga AC, et al. Improved detection suggests all Merkel cell carcinomas harbor Merkel polyomavirus. *J Clin Invest* 2012;122:4645–53.
- Sato S, Ikeda K, Shioi G, Nakao K, Yajima H, Kawakami K. Regulation of Six1 expression by evolutionarily conserved enhancers in tetrapods. *Dev Biol* 2012;368:95–108.
- Sato T, Kaneda A, Tsuji S, Isagawa T, Yamamoto S, Fujita T, et al. PRC2 overexpression and PRC2-target gene repression relating to poorer prognosis in small cell lung cancer. *Sci Rep* 2013;3:1911.
- Shah AM, Krohn P, Baxi AB, Tavares ALP, Sullivan CH, Chillakuru YR, et al. Six1 proteins with human branchio-oto-renal mutations differentially affect cranial gene expression and otic development. *Dis Model Mech* 2020;13:dmm043489.
- Song L, Bretz AC, Gravemeyer J, Spassova I, Muminova S, Gambichler T, et al. The HDAC inhibitor domatinostat promotes cell-cycle arrest, induces apoptosis, and increases immunogenicity of Merkel cell carcinoma cells. *J Invest Dermatol* 2021;141:903–12.e4.
- Starrett GJ, Thakuria M, Chen T, Marcelus C, Cheng J, Nomburg J, et al. Clinical and molecular characterization of virus-positive and virus-negative Merkel cell carcinoma. *Genome Med* 2020;12:30.
- Suen AA, Jefferson WN, Wood CE, Williams CJ. SIX1 regulates aberrant endometrial epithelial cell differentiation and cancer latency following developmental estrogenic chemical exposure. *Mol Cancer Res* 2019;17:2369–82.
- Tang CK, Toker C. Trabecular carcinoma of the skin: an ultrastructural study. *Cancer* 1978;42:2311–21.
- Ugurel S, Spassova I, Wohlfarth J, Drusio C, Cherouny A, Melior A, et al. MHC class-I downregulation in PD-1/PD-L1 inhibitor refractory Merkel cell carcinoma and its potential reversal by histone deacetylase inhibition: a case series. *Cancer Immunol Immunother* 2019;68:983–90.
- Van Mierlo G, Veenstra GJC, Vermeulen M, Marks H. The complexity of PRC2 subcomplexes. *Trends Cell Biol* 2019;29:660–71.
- Veijia T, Koljonen V, Bohling T, Kero M, Knuutila S, Sarhadi VK. Aberrant expression of ALK and EZH2 in Merkel cell carcinoma. *BMC Cancer* 2017;17:236.
- Wilson BG, Wang X, Shen X, McKenna ES, Lemieux ME, Cho YJ, et al. Epigenetic antagonism between polycomb and SWI/SNF complexes during oncogenic transformation [published correction appears in *Cancer Cell* 2011;19:153] *Cancer Cell* 2010;18:316–28.
- Wong SQ, Waldeck K, Vergara IA, Schröder J, Madore J, Wilmott JS, et al. UV-associated mutations underlie the etiology of MCV-negative Merkel cell carcinomas. *Cancer Res* 2015;75:5228–34.
- Yan N, Cheng L, Cho K, Malik MTA, Xiao L, Guo C, et al. Postnatal onset of retinal degeneration by loss of embryonic Ezh2 repression of Six1. *Sci Rep* 2016;6:33887.
- Yu HV, Tao L, Llamas J, Wang X, Nguyen JD, Trecek T, et al. POU4F3 pioneer activity enables ATOH1 to drive diverse mechanoreceptor differentiation through a feed-forward epigenetic mechanism. *Proc Natl Acad Sci USA* 2021;118:e2105137118.
- Zhou H, Blevins MA, Hsu JY, Kong D, Galbraith MD, Goodspeed A, et al. Identification of a small-molecule inhibitor that disrupts the SIX1/EYA2 complex, EMT, and metastasis. *Cancer Res* 2020;80:2689–702.

## SUPPLEMENTARY MATERIALS AND METHODS

### Tissue culture

293T, G401, and A549 cells were obtained from ATCC (Manassas, VA). Established Merkel cell carcinoma cell lines were gifts from Masahiro Shuda (University of Pittsburgh, Pittsburgh, PA), Jürgen Becker (University Duisburg-Essen, Duisburg, Germany), and Roland Houben (University Hospital Würzburg, Würzburg, Germany). MCC301, MCC336, and MCC350 were gifts from Catherine Wu (Dana-Farber Cancer Institute). MKL-1, WaGa, and UISO were validated by short tandem repeat analysis in October 2019 before beginning this study and found to be identical to previous profiling by [Daily et al., 2015](#). MKL-1 was also identical to profiling by the European Collection of Authenticated Cell Cultures. MKL-2, MS-1, PeTa, MCC13, MCC26, 293T, G401, and A549 were not validated. Short tandem repeat analysis indicated that MCC301, MCC336, and MCC350 were pure, nonidentical cell lines with a maximum of two alleles each. All cells tested negative for mycoplasma before beginning this study and at 6-month intervals throughout the study by PCR (Bulldog-Bio, Portsmouth, NH).

### Generation of plasmid constructs and cell line transduction

*SIX1* constructs were generated with pLIX\_402 (a gift from David Root; 41394, Addgene, Watertown, MA). To generate single guide RNA constructs, Lenti-multi-CRISPR (a gift from Qin Yan; 85402, Addgene) was PCR amplified with each primer pair mentioned in [Supplementary Table S15](#) and cloned as described by [Cao et al., 2016](#). Two guides were cloned into each construct and two independent constructs were generated per gene. To generate lentivirus, except for the CRISPR library, 293T cells were transfected using polyethyleneimine with expression constructs, psPAX2, and pMD2.G (gifts from Didier Trono; 12260/12259, Addgene). For the CRISPR library, 293T cells were transfected with X-tremeGENE HP DNA transfection reagent (MilliporeSigma, Burlington, MA). MKL-1 or MCC13 were spinfected at 931g for 2 hours at room temperature with 2 µg/ml polybrene, after which 1 volume of media was added. To generate the cell lines and polyclonal knockouts, media was changed the next day and selection began immediately. For the CRISPR screen, media was changed the next day and selection began on day 3 after spinfection. All cells were selected with 1.5 µg/ml puromycin (GoldBio Technology, St. Louis, MO) for 3 days. For the polyclonal knockout experiments, cells were transduced separately for each replicate and tazemetostat treatment began immediately after removal of selection.

### Cell proliferation assays

For each line, equal cell numbers were plated per drug concentration. MKL-1 and MCC13 were treated with 1% ethanol or EPZ011989 and WaGa and MCC26 were treated with 1% DMSO or tazemetostat. Cells were treated with Accutase to disrupt cell clumps (MKL-1), triturated (WaGa), or trypsinized (Thermo Fisher Scientific, Waltham, MA; MCC13, MCC26) every 3 days for counting and splitting according to the needs of each line's vehicle condition.

### Cell-cycle analysis

MKL-1 and MCC13 cells were plated in 1% ethanol or 3 µM EPZ011989 for 6 and 12 days with refreshment and splitting

every 3 days to prevent media depletion or contact inhibition. On day 6 and 12, cells were labeled with 10 µM 5-ethynyl-2'-deoxyuridine (Thermo Fisher Scientific) in 0.1% DMSO for 1 hour. MKL-1 cells were dissociated with Accutase and MCC13 cells were trypsinized, and equal cell numbers per sample (2 million for MKL-1 on both days and 1 million or 330,000 for MCC13 on day 6 and day 12, respectively) were fixed in -20 °C 70% ethanol. Alexa Fluor-647 azide (Click Chemistry Tools, Scottsdale, AZ) was conjugated onto DNA-incorporated 5-ethynyl-2'-deoxyuridine by copper-catalyzed click chemistry. Cells were stained with DAPI (MilliporeSigma) to measure total DNA and passed through a 70-µm filter. Flow cytometry was used for cell-cycle analysis. Doublets were removed by DAPI height versus area discrimination, and a minimum 30,000 events were recorded per sample. Gates were drawn separately for each cell line and applied to both vehicle and EPZ011989-treated samples.

### RT-qPCR

MKL-1 were treated in triplicate with 1% ethanol or 3 µM EPZ011989 for 6 and 12 days with refreshment every 3 days. Pellets were extracted with TRIzol/chloroform. Reverse transcription was carried out with the High-Capacity cDNA Reverse Transcription Kit (Thermo Fisher Scientific). RT-qPCR was performed using Brilliant III Ultra-Fast Sybr Green QPCR Master Mix (Agilent Technologies, Santa Clara, CA) with 40 cycles of two-step amplification and melting temperature of 60 °C. Primers are shown in [Supplementary Table S15](#).  $\Delta\Delta C_t$  analysis was used with normalization to 18S rRNA, and then to day 6 vehicle. Confidence intervals for each biological replicate were calculated as maximum/minimum fold change from the SDs of the technical replicates and were averaged for the final graphed confidence interval. A two-way ANOVA was performed for each gene using the biological replicate  $\Delta C_t$  values.

### Microscopy

Images were taken at  $\times 4$  or  $\times 10$  using SPOT5.2 software on a Nikon Eclipse TE300 inverted microscope (Nikon, Tokyo, Japan) with a Diagnostic Instruments Model #25.4 2 megapixel Slider Camera (Diagnostic Instruments, Sterling Heights, MI).

### RNA sequencing and analysis

Novogene Corporation Inc. (Durham, NC) performed polyA selection, library preparation, and sequencing on the NovaSeq 6000 (Illumina, Inc., San Diego, CA) to >6G data per sample of PE150 reads. Sequence quality was assessed by FastQC ([Andrews, 2010](#)). Sequences were aligned with Salmon ([Patro et al., 2017](#)) to the GRCH38p.13 v101 cDNA library with GRCH38p.13 v101 gDNA used as a decoy. Differential expression analysis was performed using DESeq2 ([Love et al., 2014](#)). Analysis was restricted to transcripts with a HUGO Gene Nomenclature Committee symbol. Gene Ontology analyses were performed using DAVID ([Huang et al., 2009a; Huang et al., 2009b](#)).

### CUT&RUN sequencing and analysis

The Dana-Farber Cancer Institute Molecular Biology Core Facilities performed library preparation by automated Swift 2S ligation chemistry (Integrated DNA Technologies, Newark, NJ) and sequencing on the NovaSeq 6000 to >13M PE100 reads per sample. Sequence quality was assessed by FastQC.

Read pairs were aligned with Bowtie 2 (Langmead and Salzberg, 2012) to GRCh38 and *E. coli* K-12 GCA\_004919995 with options: `-local -very-sensitive-local -no-unal -no-mixed -no-discordant -phred33 -I 10 -X 700`. SAMtools (Li et al., 2009) view was used to downsample the aligned human reads according to the aligned *E. coli* reads per sample. Peak calling for the histone H3 lysine 4 trimethyl and IgG samples used the following MACS2 (Zhang et al., 2008) options: `-q 0.05 -keep-dup all -nolambda`. NarrowPeak files were used for analysis. The same commands were used for histone H3 lysine 27 trimethyl samples with the addition of options: `-broad -broad-cutoff 0.1`. BroadPeak files were used for analysis. Heatmaps were generated with `computeMatrix` and `plotHeatmap` from deepTools (Ramírez et al., 2014). NarrowPeak and BroadPeak files were analyzed by ChIPpeakAnno (Zhu et al., 2010). Only peaks that mapped to the autosomes or X or Y chromosomes were retained. Among these, only peaks that overlapped in the replicates were considered high quality and further analyzed (Supplementary Figure S9b and S10b). Peaks were annotated with TxDb.Hsapiens.UCSC.hg38.knownGene, and only peaks that were annotated to promoters (−2,000 to +500 base pairs from transcription start site) were analyzed (Supplementary Figure S11). These peaks were annotated to genes using `annotatePeakInBatch` with `EnsDb.Hsapiens.v86` and options to only include peaks overlapping promoters. Annotations were refined to only genes with Ensembl gene identifications and HUGO Gene Nomenclature Committee symbols.

To obtain bivalent to active genes, `findOverlapsOfPeaks` was first used on the lists of promoter-associated vehicle histone H3 lysine 27 trimethyl and histone H3 lysine 4 trimethyl peaks. This gave a new list of genome coordinates encompassing the overlapping peaks, and these coordinates were examined in the Figure 3a heatmap. `findOverlapsOfPeaks` was used again to compare these coordinates with the EPZ011989 histone H3 lysine 4 trimethyl promoter-associated peaks and obtain a list of genome coordinates encompassing overlaps of all three sets of peaks. This was then annotated with `annotatePeakInBatch` as before to obtain the bivalent to active gene list (Supplementary Table S7). Gene Ontology analyses were performed on this list using DAVID. To integrate the RNA sequencing and CUT&RUN, genes were classified by the presence or absence of each mark in promoters as shown in Supplementary Table S9 (i.e., the gene appeared or did not appear in the annotation lists for promoter-associated peaks of each mark as shown in Supplementary Tables S4–6).

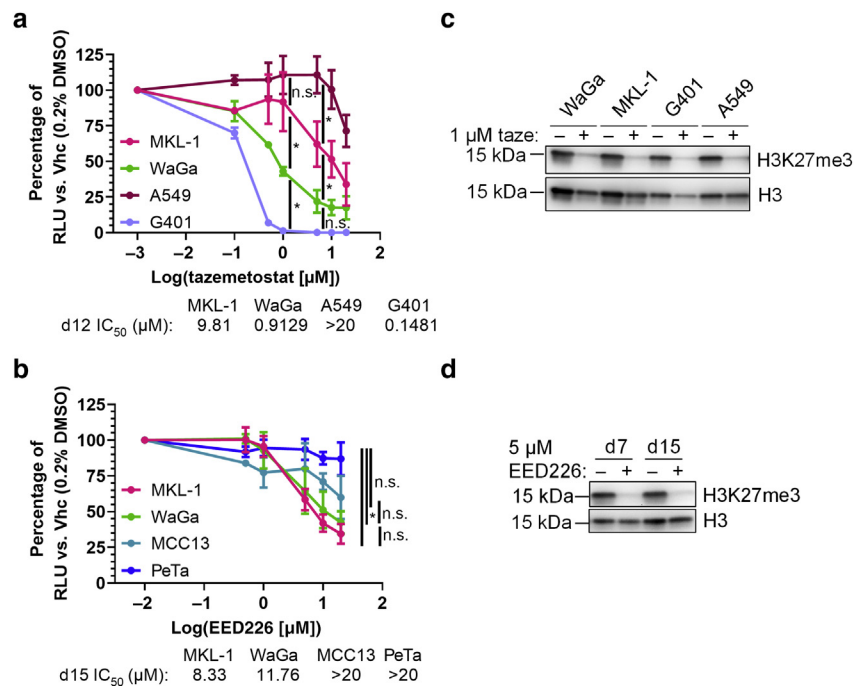
### CRISPR screen sequencing and analysis

Sequencing was performed by Novogene Corporation Inc. on the NovaSeq 6000 to obtain >30 million PE150 reads.

Sequence quality was assessed by FastQC. Only read 1 was used for analysis as recommended by the Addgene H3 library protocol. MAGeCK-MLE was used to identify differential abundance of guides in each sample (Li et al., 2015). As recommended, built-in control guides targeting *AAVS1*, *CCR5*, and *ROSA26* were used for normalization. CTRL guides were not used. Copy number correction was performed using a previously published input dataset from chromatin immunoprecipitation sequencing of MKL-1 (Cheng et al., 2017). Further analyses were performed with MAGeCKFlute using the recommended cell-cycle normalization of beta scores (Wang et al., 2019).

### SUPPLEMENTARY REFERENCES

- Andrews S. FastQC: A quality control tool for high throughput sequence data, <http://www.bioinformatics.babraham.ac.uk/projects/fastqc>; 2010 (accessed 29 October 2021).
- Cao J, Wu L, Zhang SM, Lu M, Cheung WKC, Cai W, et al. An easy and efficient inducible CRISPR/Cas9 platform with improved specificity for multiple gene targeting. *Nucleic Acids Res* 2016;44:e149.
- Cheng J, Park DE, Berrios C, White EA, Arora R, Yoon R, et al. Merkel cell polyomavirus recruits MYCL to the EP400 complex to promote oncogenesis. *PLoS Pathog* 2017;13:e1006668.
- Daily K, Coxon A, Williams JS, Lee CCR, Coit DG, Busam KJ, et al. Assessment of cancer cell line representativeness using microarrays for Merkel cell carcinoma. *J Invest Dermatol* 2015;135:1138–46.
- Huang DW, Sherman BT, Lempicki RA. Bioinformatics enrichment tools: paths toward the comprehensive functional analysis of large gene lists. *Nucleic Acids Res* 2009a;37:1–13.
- Huang DW, Sherman BT, Lempicki RA. Systematic and integrative analysis of large gene lists using DAVID bioinformatics resources. *Nat Protoc* 2009b;4:44–57.
- Langmead B, Salzberg SL. Fast gapped-read alignment with Bowtie 2. *Nat Methods* 2012;9:357–9.
- Li H, Handsaker B, Wysoker A, Fennell T, Ruan J, Homer N, et al. The sequence alignment/map format and SAMtools. *Bioinformatics* 2009;25:2078–9.
- Li W, Köster J, Xu H, Chen CH, Xiao T, Liu JS, et al. Quality control, modeling, and visualization of CRISPR screens with MAGeCK-VISPR. *Genome Biol* 2015;16:281.
- Love MI, Huber W, Anders S. Moderated estimation of fold change and dispersion for RNA-seq data with DESeq2. *Genome Biol* 2014;15:550.
- Patro R, Duggal G, Love MI, Irizarry RA, Kingsford C. Salmon: fast and bias-aware quantification of transcript expression using dual-phase interference. *Nat Methods* 2017;14:417–9.
- Ramírez F, Dündar F, Diehl S, Grüning BA, Manke T. DeepTools: a flexible platform for exploring deep-sequencing data. *Nucleic Acids Res* 2014;42:W187–91.
- Wang B, Wang M, Zhang W, Xiao T, Chen CH, Wu A, et al. Integrative analysis of pooled CRISPR genetic screens using MAGeCKFlute. *Nat Protoc* 2019;14:756–80.
- Zhang Y, Liu T, Meyer CA, Eeckhoutte J, Johnson DS, Bernstein BE, et al. Model-based analysis of ChIP-seq (MACS). *Genome Biol* 2008;9:R137.
- Zhu LJ, Gazin C, Lawson ND, Pagès H, Lin SM, Lapointe DS, et al. ChIPpeakAnno: a Bioconductor package to annotate ChIP-seq and ChIP-chip data. *BMC Bioinformatics* 2010;11:237.

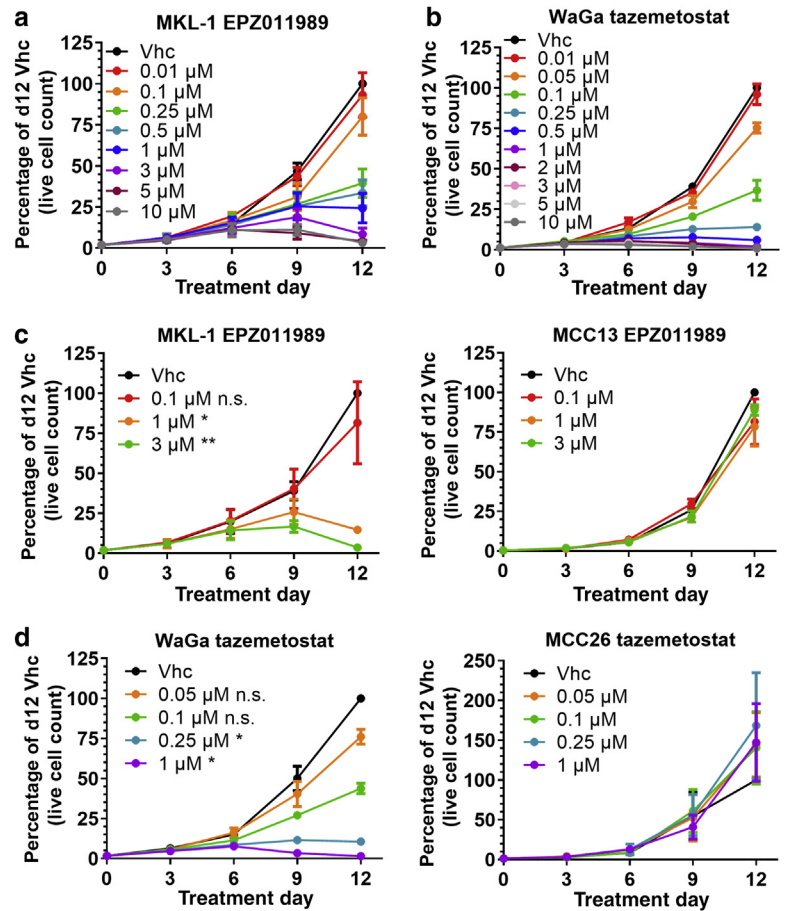


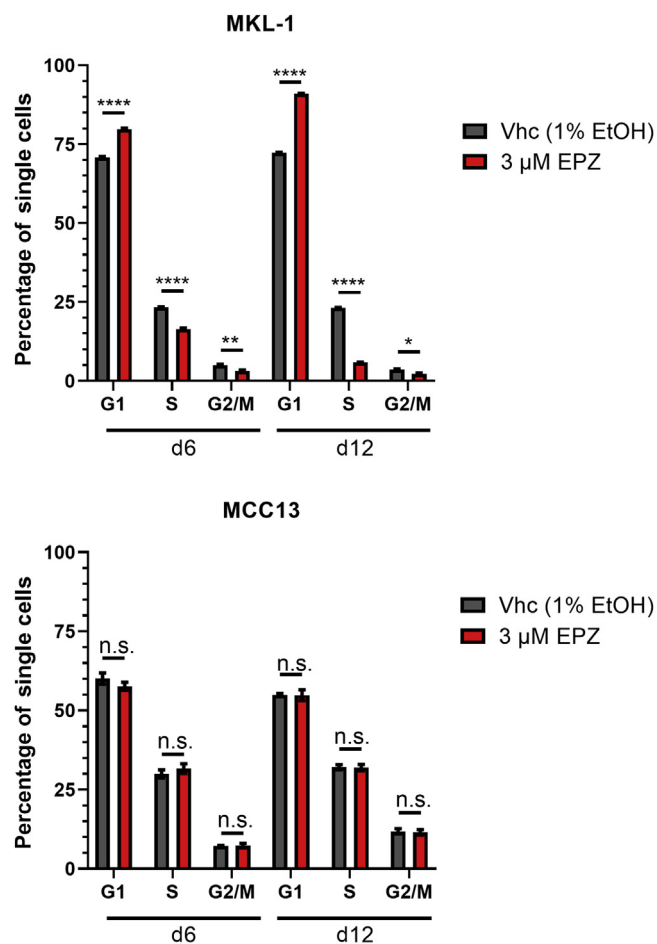
**Supplementary Figure S1. Comparison of MCC and non-MCC cell line responses to tazemetostat and characterization of MCC responses to EED226.**

(a) 12-day CellTiter-Glo assay comparing tazemetostat sensitivity of MCC cell lines with the EZH2i-sensitive and -resistant cell lines G401 and A549. N = 2; mean  $\pm$  SD; two-way ANOVA with Tukey's posthoc tests for selected comparisons at 1 and 5  $\mu$ M; \* $P$  < 0.05. (b) 15-day CellTiter-Glo assay of tazemetostat-sensitive and -resistant MCC cell lines treated with EED226. N = 2; mean  $\pm$  SD; two-way ANOVA with Tukey's posthoc tests for selected comparisons at 10  $\mu$ M; \* $P$  < 0.05; similar posthoc results at 5  $\mu$ M. (c) Immunoblots of histones from cells treated with 1  $\mu$ M tazemetostat for 6 days. Representative of two experiments. (d) Immunoblots of histones from MKL-1 treated with 5  $\mu$ M EED226 for 7 or 15 days. Representative of two experiments. d, day; H3K27me3, histone H3 lysine 27 trimethylation; IC<sub>50</sub>, half-maximal inhibitory concentration; EZH2i, EZH2 inhibitor; MCC, Merkel cell carcinoma; n.s., nonsignificant; RLU, relative light unit; taze, tazemetostat; vhc, vehicle; vs., versus.

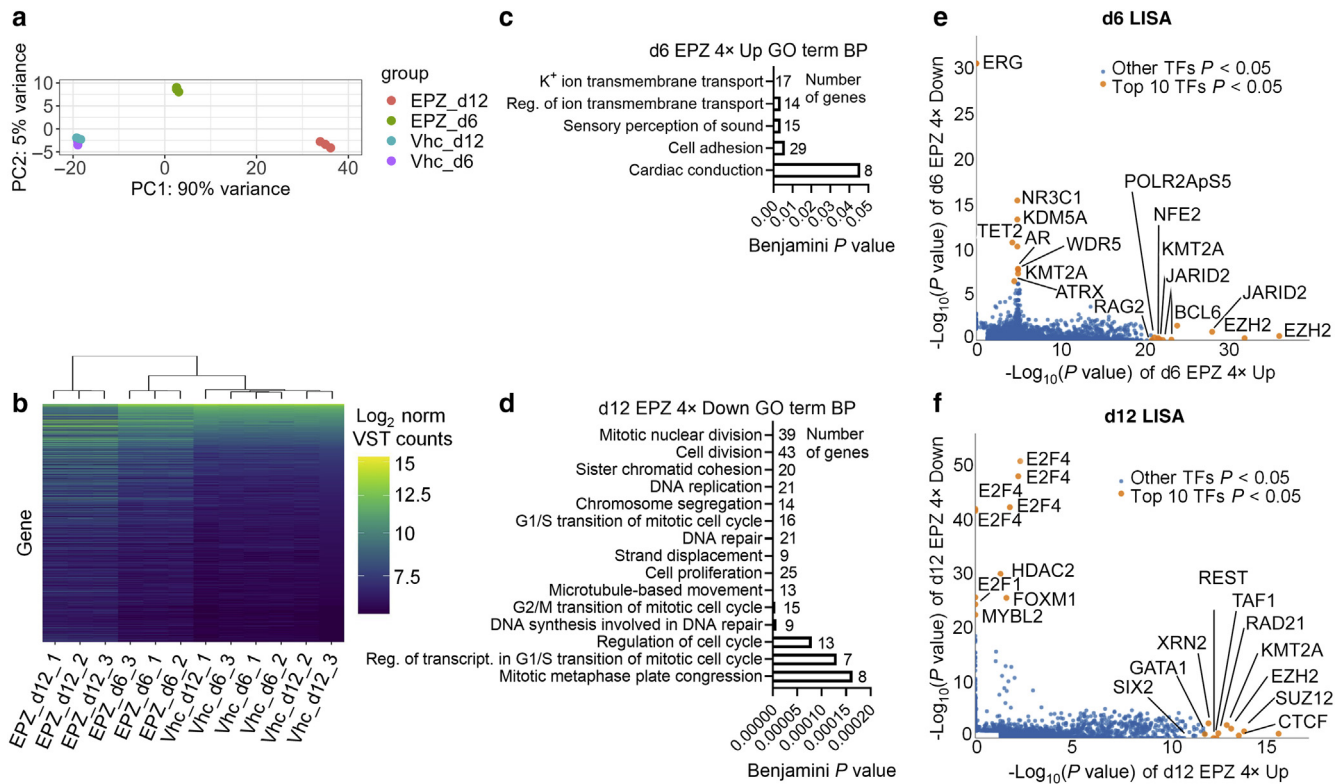
**Supplementary Figure S2. Cell proliferation assays of MCC cell lines treated with EZH2 inhibitors.**

(a) A 12-day proliferation assay of EPZ011989-treated MKL-1 and of (b) tazemetostat-treated WaGa. N = 3; mean  $\pm$  SEM. (c) A 12-day proliferation assay of MKL-1 and MCC13 cells treated side-by-side with EPZ011989. N = 3; mean  $\pm$  SEM; two-way ANOVA comparing MKL-1 and MCC13 day 12 responses at each dose with Šídák's posthoc tests; \* $P$  < 0.05; \*\* $P$  < 0.01. (d) A 12-day proliferation assay of WaGa and MCC26 treated side-by-side with tazemetostat. N = 3; mean  $\pm$  SEM; two-way ANOVA comparing WaGa and MCC26 day 12 responses at each dose with Šídák's posthoc tests; \* $P$  < 0.05. d, day; MCC, Merkel cell carcinoma; n.s., nonsignificant; vhc, vehicle.

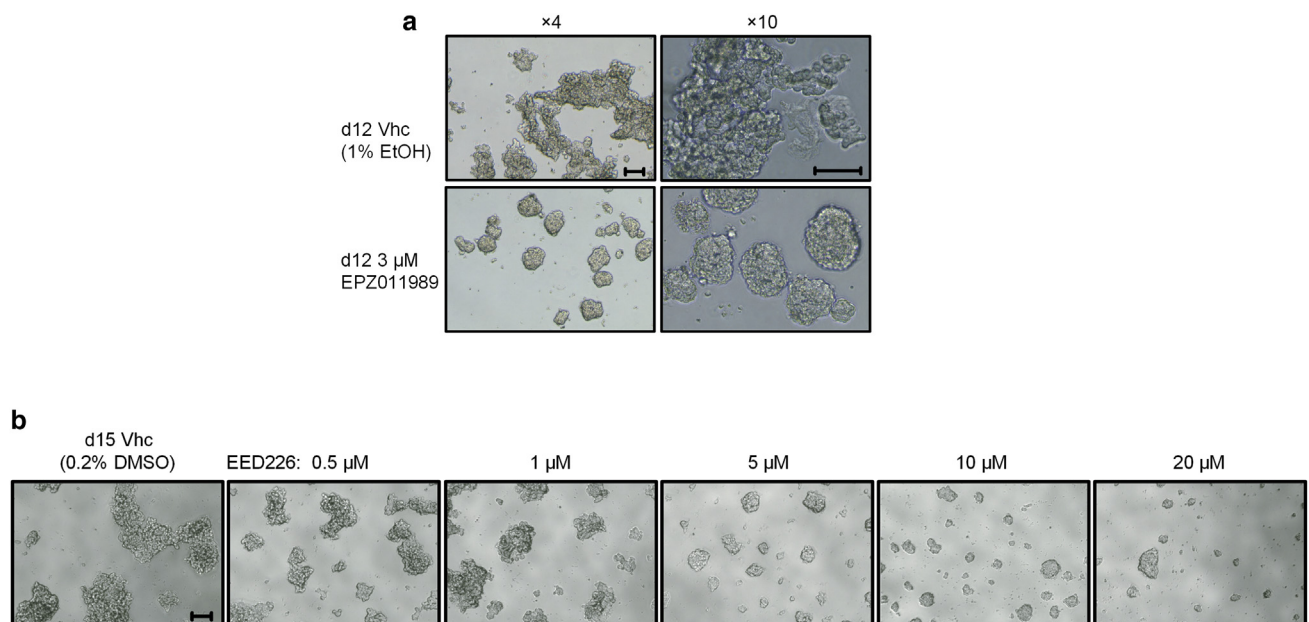




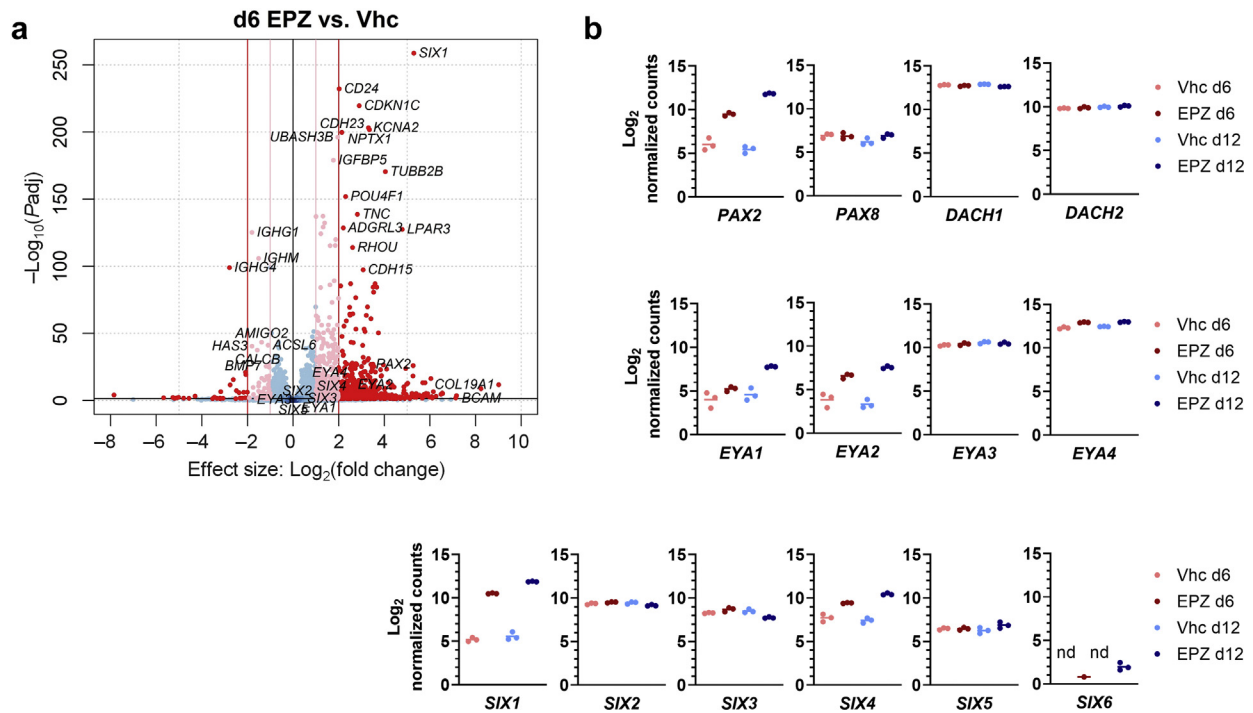
**Supplementary Figure S3. Cell-cycle analyses of MCC cell lines treated with EPZ011989.** MKL-1 and MCC13 were treated side-by-side with vehicle or 3 μM EPZ011989 for 6 and 12 days and analyzed for cell-cycle distributions. N = 3; mean ± SEM; two-way ANOVA for each cell-cycle phase within each cell line with Šídák's posthoc tests; \* $P < 0.05$ ; \*\* $P < 0.01$ ; \*\*\*\* $P < 0.0001$ . d, day; EPZ, EPZ011989; EtOH, ethanol; MCC, Merkel cell carcinoma; n.s., nonsignificant; vhc, vehicle.



**Supplementary Figure S4. RNA sequencing quality control and analysis of upregulated and downregulated gene sets after EPZ011989 treatment.** (a) Principle component analysis plot of RNA sequencing replicates after 6- or 12-day treatment of MKL-1 with vehicle or 3  $\mu$ M EPZ011989. (b) Hierarchical clustering of samples plotting log<sub>2</sub> normalized variance-stabilizing transformed counts for all four-fold DEGs (absolute log<sub>2</sub>FC  $\geq 2$ ,  $P_{adj} \leq 0.05$ ). (c) GO term BP analysis of day 6 four-fold upregulated DEGs. (d) GO term BP analysis of day 12 four-fold downregulated DEGs. (e) Epigenetic landscape in silico deletion analysis of the top 500 four-fold upregulated and downregulated DEGs on day 6 and (f) on day 12 using publicly available transcription factor chromatin immunoprecipitation sequencing datasets. adj, adjusted; BP, biological process; d, day; DEG, differentially expressed gene; down, downregulated; EPZ, EPZ011989; FC, fold change; GO, Gene Ontology; K<sup>+</sup>, potassium; LISA, epigenetic landscape in silico deletion analysis; PC, principal component; reg., regulation; TF, transcription factor; transcript., transcription; up, upregulated; vhc, vehicle; VST, variance-stabilizing transformed.

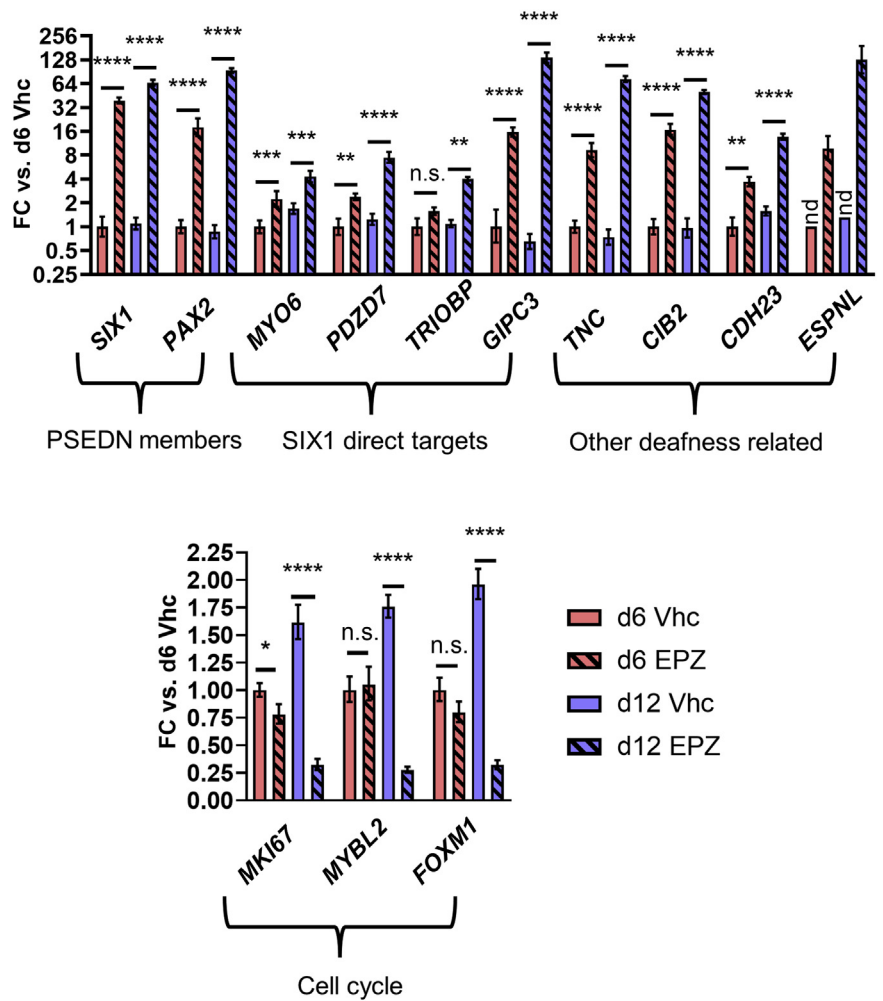


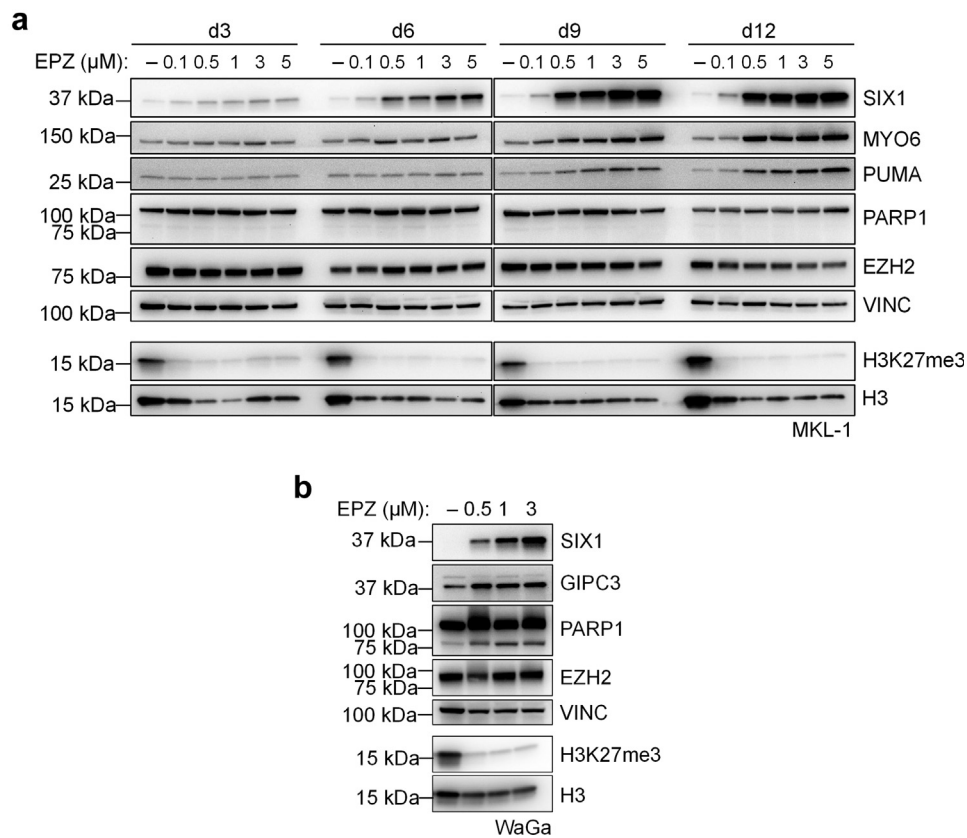
**Supplementary Figure S5. Morphological changes of MKL-1 treated with EPZ011989 and EED226.** (a) MKL-1 treated with vehicle formed loosely-associated sheet-like clumps, whereas those treated with 3  $\mu$ M EPZ011989 for 12 days or (b) doses of EED226 for 15 days formed similar-looking, tightly-associated clumps. Bar = 100  $\mu$ m. Magnification  $\times 4$  and  $\times 10$  in **a**;  $\times 4$  in **b**. **a** is representative of three experiments; **b** of two. d, day; EtOH, ethanol; vhc, vehicle.



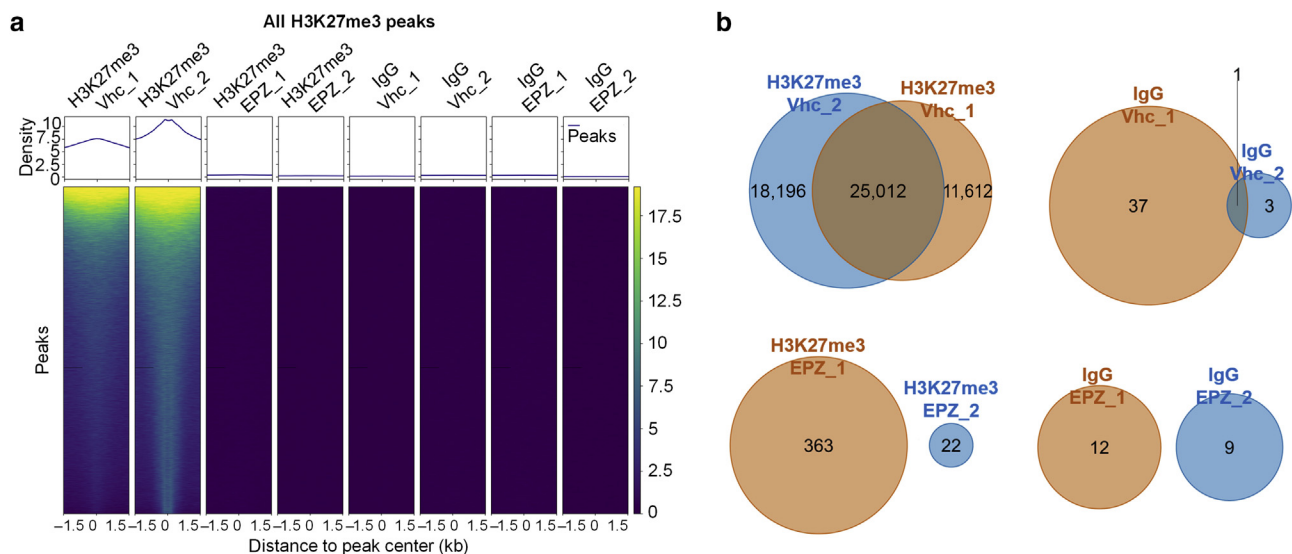
**Supplementary Figure S6. RNA sequencing analysis of day 6 DEGs and selected PSEDN transcription factors after EPZ011989 treatment.** (a) Volcano plot highlighting two-fold (pink) and four-fold (red) significant upregulated and downregulated genes after 6-day treatment of MKL-1 with 3  $\mu\text{M}$  EPZ011989. (b) Normalized counts of PSEDN transcription factors in each RNA sequencing condition. Mean + individual replicates. d, day; DEG, differentially expressed gene; EPZ, EPZ011989; nd, not detected; PSEDN, PAX-SIX-EYA-DACH network; vhc, vehicle; vs., versus.

**Supplementary Figure S7. RT-qPCR validation of expression changes identified by RNA sequencing after EPZ011989 treatment.** MKL-1 were treated with vehicle or 3  $\mu$ M EPZ011989 for 6 and 12 days.  $\Delta\Delta$ Ct normalization to 18S rRNA and day 6 vehicle; N = 3; mean + confidence interval from technical replicate SD; two-way ANOVA for each gene with Bonferroni posthoc tests; \* $P$  < 0.05; \*\* $P$  < 0.01; \*\*\* $P$  < 0.001; \*\*\*\* $P$  < 0.0001. *ESPNL* not detected in vehicle conditions and Ct was set to 40 to permit FC calculation. d, day; EPZ, EPZ011989; FC, fold change; nd, not detected; n.s., nonsignificant; PSEDN, PAX-SIX-EYA-DACH network; vhc, vehicle; vs. versus.

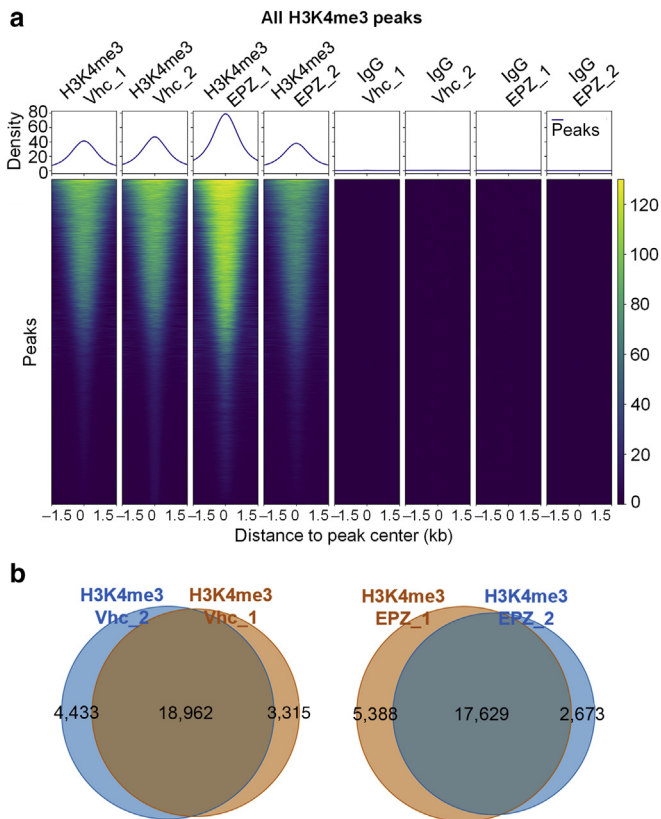




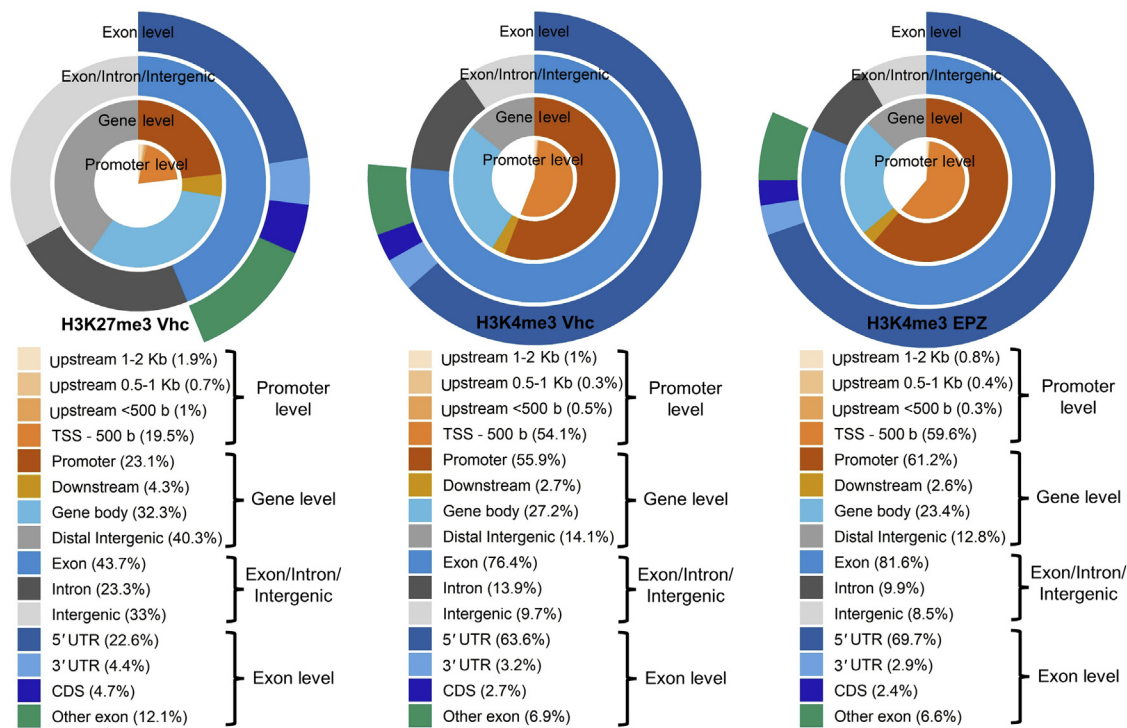
**Supplementary Figure S8. Analysis of dose- and time-dependent activity of EPZ011989 on H3K27me3 and SIX1 and its targets.** (a) Immunoblots of MKL-1 treated with doses of EPZ011989 for the indicated number of days. Nonhistone blots representative of two identical experiments; histone blots representative of two experiments where this one was harvested with acid and one with RIPA buffer. (b) RIPA buffer and histone acid immunoblots of WaGa treated with doses of EPZ011989 for 6 days. N = 1. d, day; EPZ, EPZ011989; H3K27me3, histone H3 lysine 27 trimethylation; RIPA, radioimmunoprecipitation assay.



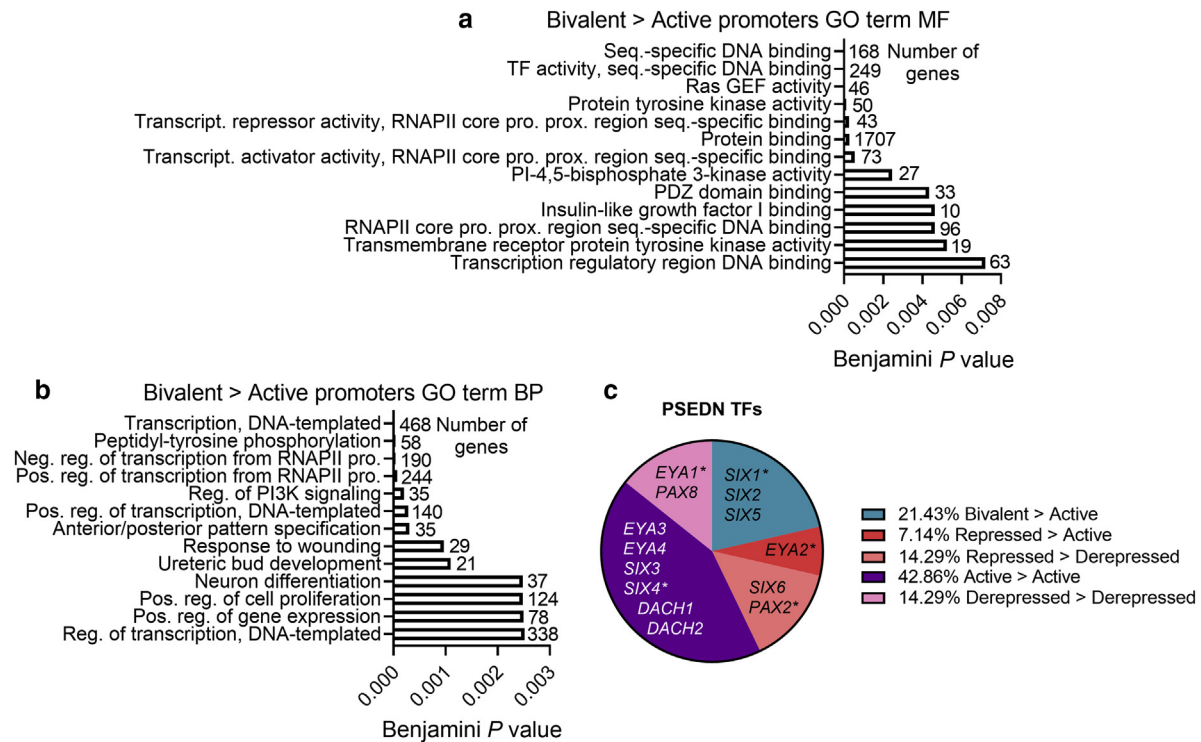
**Supplementary Figure S9. Quality control of H3K27me3 peaks identified by CUT&RUN in vehicle- and EPZ011989-treated MKL-1.** (a) Peak-centered heatmap of all H3K27me3 peaks identified in vehicle samples and corresponding regions in 3  $\mu$ M EPZ011989-treated samples bound with  $\alpha$ -H3K27me3 and samples bound with control IgG. (b) Venn diagrams showing numbers of overlapping peaks for the H3K27me3 and IgG replicates. Only overlapping peaks were considered high-quality and entered downstream annotation analyses. EPZ, EPZ011989; H3K27me3, histone H3 lysine 27 trimethylation; kb, kilobase; vhc, vehicle.



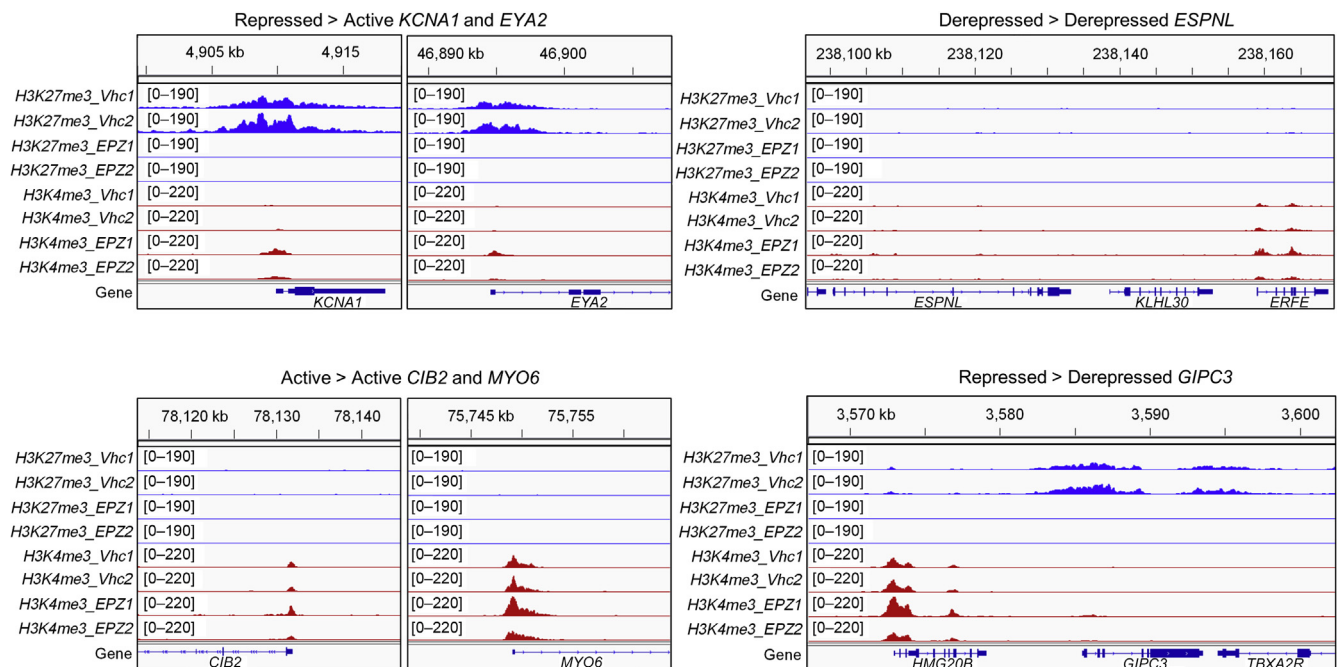
**Supplementary Figure S10. Quality control of H3K4me3 peaks identified by CUT&RUN in vehicle- and EPZ011989-treated MKL-1.** (a) Peak-centered heatmap of all H3K4me3 peaks identified in vehicle samples and corresponding regions in 3  $\mu$ M EPZ011989-treated samples bound with  $\alpha$ -H3K4me3 and samples bound with control IgG. (b) Venn diagrams showing numbers of overlapping peaks for the H3K4me3 replicates. Only overlapping peaks were considered high-quality and entered downstream annotation analyses. EPZ, EPZ011989; H3K4me, histone H3 lysine 4 trimethylation; kb, kilobase; vhc, vehicle.



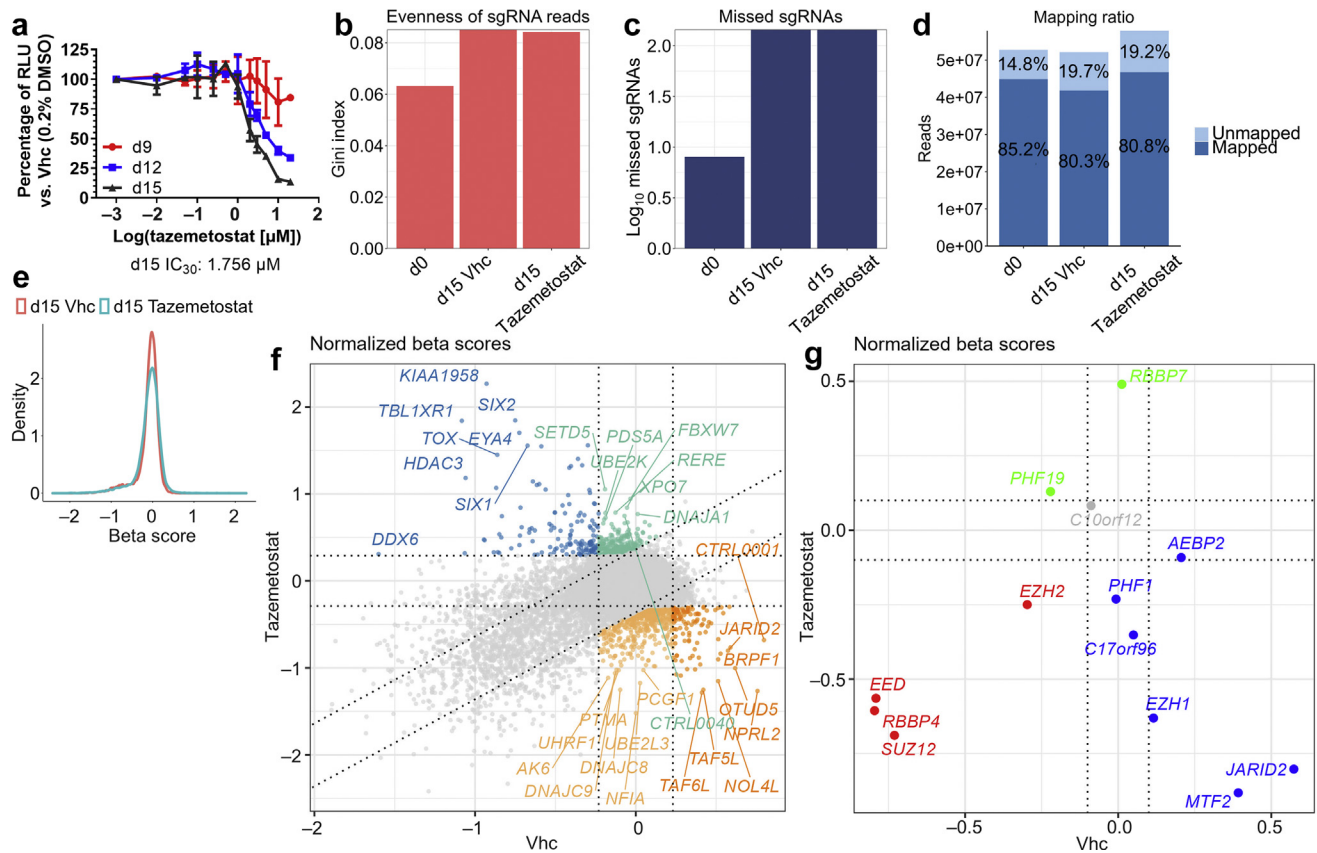
**Supplementary Figure S11. Annotation of H3K27me3 and H3K4me3 peaks to genomic features in vehicle- and EPZ011989-treated CUT&RUN samples.** Only overlapping peaks shown in Supplementary Figure S9b and Supplementary Figure S10b were analyzed. Peaks annotated at the gene level to promoters entered downstream analyses for annotation to specific genes or examination of bivalent promoters in Figure 3a. b, base pairs; CDS, coding sequence; EPZ, EPZ011989; H3K27me3, histone H3 lysine 27 trimethylation; H3K4me3, histone H3 lysine 4 trimethylation; kb, kilobase; TSS, transcription start site; UTR, untranslated region; vhc, vehicle.



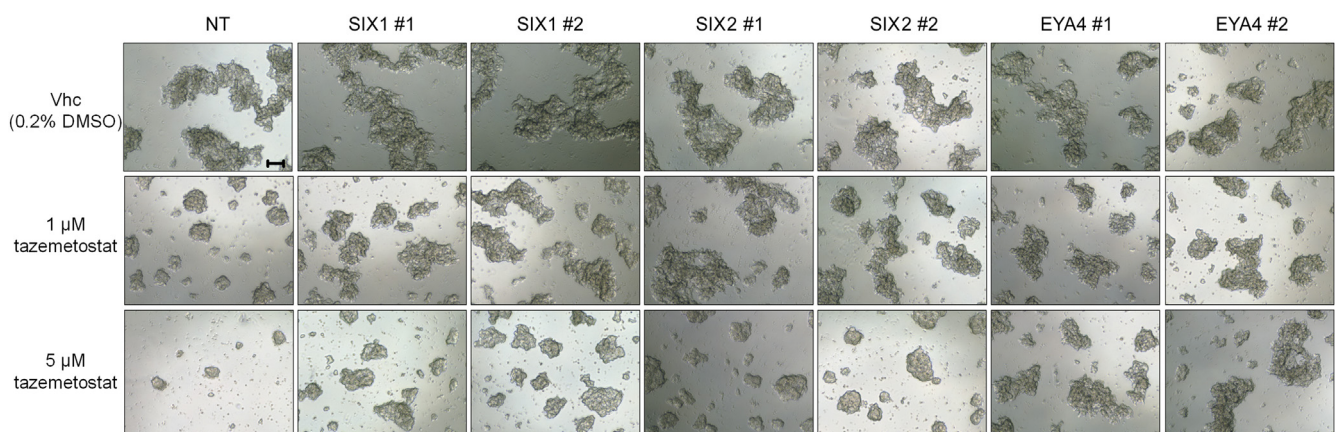
**Supplementary Figure S12. Gene-level analysis of promoter-associated H3K27me3 and H3K4me3 peaks identified in vehicle- and EPZ011989-treated CUT&RUN samples.** (a) GO term MF and (b) BP analysis of bivalent to active genes (i.e., genes with overlapping promoter-associated H3K27me3/H3K4me3 peaks in vehicle and H3K4me3 peaks in the EPZ011989 condition) identified by CUT&RUN. (c) Promoter classification of selected PSEDN transcription factors according to presence or absence of promoter-associated H3K27me3 and H3K4me3 peaks as shown in [Supplementary Table S9](#). \*Gene was also at least two-fold upregulated in the day 6 RNA sequencing results. BP, biological process; GO, Gene Ontology; H3K27me3, histone H3 lysine 27 trimethylation; H3K4me3, histone H3 lysine 4 trimethylation; MF, molecular function; neg. reg., negative regulation; PI, phosphatidylinositol; pos. reg., positive regulation; pro., promoter; prox., proximal; PSEDN, PAX-SIX-EYA-DACH network; reg., regulation; seq., sequence; TF, transcription factor; transcript., transcriptional.



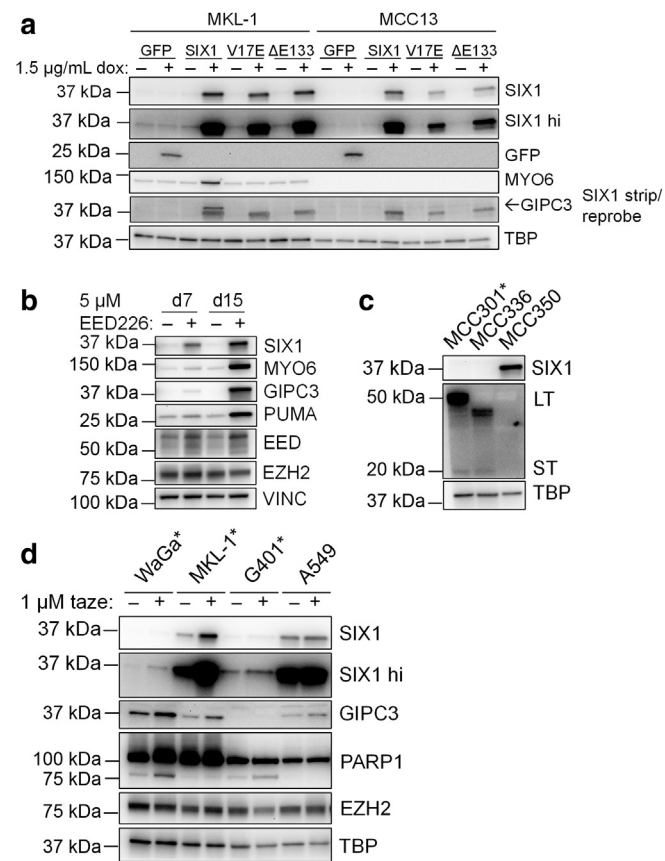
**Supplementary Figure S13. Promoter-associated H3K27me3 and H3K4me3 peaks for representative two-fold upregulated DEGs after EPZ011989 treatment.** The 1,059 two-fold upregulated DEGs on day 6 were classified according to presence/absence of promoter peaks ([Supplementary Table S9](#); [Figure 3b](#)). Representative genes from the most abundant promoter classes after the bivalent to active class are shown. DEG, differentially expressed gene; EPZ, EPZ011989; H3K27me3, histone H3 lysine 27 trimethylation; H3K4me3, histone H3 lysine 4 trimethylation; kb, kilobase; vhc, vehicle.



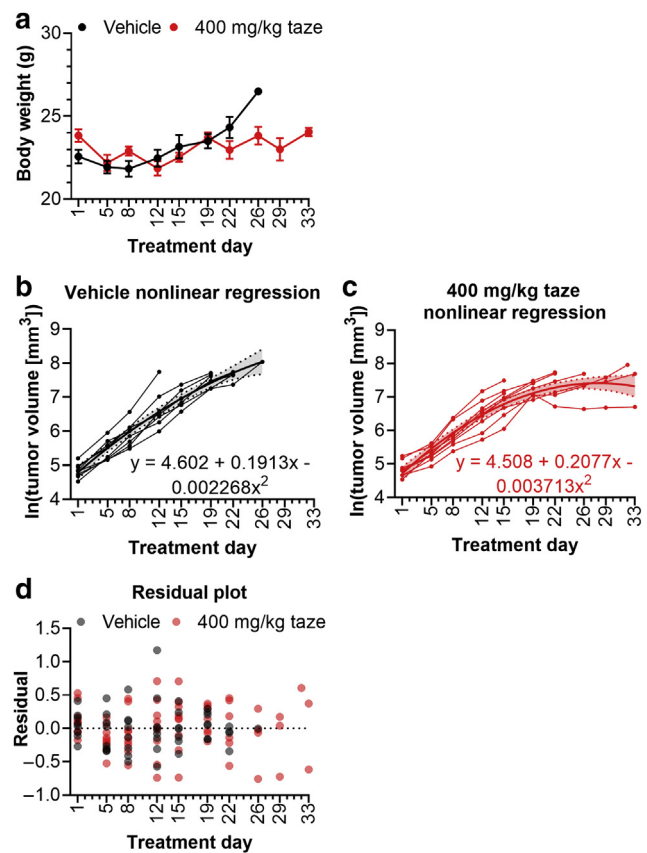
**Supplementary Figure S14. CRISPR screen quality control and beta score analysis.** (a) CellTiter-Glo assay used to calculate the tazemetostat day 15 IC<sub>30</sub> in MKL-1. N = 2; mean ± SD. (b) Gini indices and (c) zero-count sgRNAs for each screen sample. (d) Numbers/percentages of sequenced reads mapped to the H3 library. (e) Cell-cycle normalized beta score distribution in day 15 vehicle- and tazemetostat-treated samples. (f) Scatterplot of cell-cycle normalized beta scores in day 15 vehicle- and tazemetostat-treated samples for each gene. (g) Scatterplot of cell-cycle normalized beta scores in day 15 vehicle- and tazemetostat-treated samples for genes encoding PRC2 core and substoichiometric subunits. Red—negative selection in both conditions. Blue—stronger negative selection in tazemetostat versus vehicle. Green—stronger positive selection in tazemetostat versus vehicle. Gray—no major difference between tazemetostat and vehicle. d, day; PRC2, Polycomb repressor complex 2; RLU, relative light unit; sgRNA, single guide RNA; vhc, vehicle.



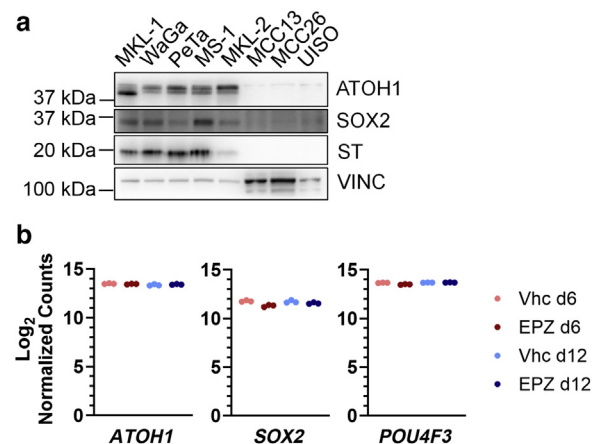
**Supplementary Figure S15. Polyclonal knockout of *SIX1*, *SIX2*, or *EYA4* dampens MKL-1 morphological changes associated with tazemetostat treatment.** Microscopy at ×4 magnification of MKL-1 transduced with the respective sgRNA constructs and treated for 15 days with vehicle or 1 or 5 μM tazemetostat. Bar = 100 μm. Representative of three experiments. #, sgRNA pair number; NT, nontargeting; sgRNA, single guide RNA; vhc, vehicle.



**Supplementary Figure S16. Additional analyses of SIX1 expression in MCC and non-MCC cell lines.** (a) Immunoblots of MKL-1 or MCC13 expressing GFP, wild-type SIX1, or a SIX1 mutant after 9 days. Control for Figure 5c. SIX1, GFP, and MYO6 representative of three experiments; GIPC3 representative of two. SIX1 hi panel shows higher exposure to highlight baseline SIX1 expression in GFP controls. (b) Immunoblots of MKL-1 treated with 5 μM EED226 for 7 or 15 days. Representative of two experiments. (c) Immunoblots of untreated patient-derived cell lines showing baseline SIX1 expression. Representative of two experiments. \*EZH2 inhibitor sensitivity. (d) Immunoblots of MCC and non-MCC cell lines treated with 1 μM tazemetostat for 6 days. Representative of 2 experiments. \*EZH2 inhibitor sensitivity. d, day; dox, doxycycline; LT, Merkel cell polyomavirus large T antigen; MCC, Merkel cell carcinoma; ST, Merkel cell polyomavirus small T antigen; taz, tazemetostat.



**Supplementary Figure S17. Additional analyses of MKL-1 xenograft experiment.** (a) Body weight measurements of mice treated with vehicle or 400 mg/kg tazemetostat twice daily. N shown for each data point in Figure 6. Mean ± SEM. (b) Least-squares nonlinear regression model calculated for vehicle-treated and (c) tazemetostat-treated tumors with overlaid individual In-transformed tumor growth curves. Shading represents 95% confidence interval. (d) Plot of the residuals of the models in b and c. One-tailed tests for homoscedasticity;  $P > 0.05$ . Anderson-Darling normality tests;  $P > 0.05$ . taz, tazemetostat.



**Supplementary Figure S18. Additional analyses of mechanosensory-related transcription factor expression in MCC cells.** (a) Immunoblots of established cell lines showing the nonviral MCC lines MCC13, MCC26, and UI50 less strongly express ATOH1 and SOX2 than the viral MCC lines. Representative of three experiments. (b) Normalized counts of mechanosensory transcription factors in each MKL-1 RNA sequencing condition showing sustained high expression. Mean with individual replicates. d, day; EPZ, EPZ011989; MCC, Merkel cell carcinoma; ST, Merkel cell polyomavirus small T antigen; vhc, vehicle.

**Supplementary Table S9. Presence/Absence of Promoter-Associated H3K27me3 and H3K4me3 Peaks Used to Define Promoter Classes**

Promoter classification	Vehicle		3 $\mu$ M EPZ011989	
	H3K27me3	H3K4me3	H3K27me3	H3K4me3
Bivalent > Active	+	+	–	+
Bivalent > Derepressed	+	+	–	–
Repressed > Active	+	–	–	+
Repressed > Derepressed	+	–	–	–
Active > Active	–	+	–	+
Active > Derepressed	–	+	–	–
Derepressed > Active	–	–	–	+
Derepressed > Derepressed	–	–	–	–

Abbreviations: H3K27me3, histone H3 lysine 27 trimethylation; H3K4me3, histone H3 lysine 4 trimethylation